

Subspace-restricted thermalization in a correlated-hopping model with strong Hilbert space fragmentation characterized by irreducible strings

Sreemayee Aditya¹, Deepak Dhar^{2*}, and Diptiman Sen¹

¹Centre for High Energy Physics, Indian Institute of Science, Bengaluru 560012, India

²Indian Institute of Science Education and Research, Dr. Homi Bhabha Road, Pashan, Pune 411008, India

We introduce a one-dimensional correlated-hopping model of spinless fermions in which a particle can hop between two neighboring sites only if the sites to the left and right of those two sites have different particle numbers. Using a bond-to-site mapping, this model involving four-site terms can be mapped to an assisted pair-flipping model involving only three-site terms. This model shows strong Hilbert space fragmentation (HSF). We define irreducible strings (IS) to label the different fragments, determine the number of fragments, and the sizes of fragments corresponding to some special IS. In some classes of fragments, the Hamiltonian can be diagonalized completely, and in others it can be seen to have a structure characteristic of models which are not fully integrable. In the largest fragment in our model, the number of states grows exponentially with the system size, but the ratio of this number to the total Hilbert space size tends to zero exponentially in the thermodynamic limit. Within this fragment, we provide numerical evidence that only a weak version of the eigenstate thermalization hypothesis (ETH) remains valid; we call this subspace-restricted ETH. To understand the out-of-equilibrium dynamics of the model, we study the infinite-temperature time-dependent autocorrelation functions starting from a random initial state; we find that these exhibit a different behavior near the boundary compared to the bulk. Finally we propose an experimental setup to realize our correlated-hopping model.

I. INTRODUCTION

Thermalization and its violation in isolated quantum systems have been studied extensively over the last several years. The strongest version of thermalization in closed quantum systems is believed to be defined by the eigenstate thermalization hypothesis (ETH)¹⁻⁴. This hypothesis states that each eigenstate in an ergodic system acts like a thermal ensemble as far as local observables are concerned, namely, local correlation functions in each eigenstate tend to the average values calculated in the quantum mechanical microcanonical ensemble at the same energy. Thus expectation values of local observables for all eigenstates for a sufficiently *large* system show “self-thermalization” on their own.

This can be further categorized into two classes called the strong and weak versions of ETH. In the first case, all of the eigenstates of a given Hamiltonian satisfy the ETH hypothesis, while in the latter case, it is obeyed by most of the eigenstates apart from some states which form a set of measure zero in the thermodynamic limit. Well-known examples where strong ETH is not valid are quantum integrable models which are either mappable to free systems^{5,6} or are solvable by the Bethe ansatz⁷⁻⁹. Strong ETH is also not satisfied in many-body localized systems which have strong disorder¹⁰⁻¹³.

In recent years, there have been a great deal of effort in identifying systems for which the strong version of ETH is not valid. One class of systems is “quantum many-body scars”¹⁴⁻¹⁹. Such systems have some special states called scar states which are highly excited and have low entanglement-entropy. If an initial state, which has a significant overlap with such eigenstates compared to other states at the same energy, is evolved in time, the long-time dynamics of correlation functions show persistent oscillations. For an quantum ergodic

system, such overlaps should be a smooth function of energy; therefore, the enhancement of overlaps for certain eigenstates compared to others is not consistent with the strong ETH. However, the presence of such states still satisfies the weak ETH with respect to the full Hilbert space since the number of scar states typically grows only polynomially with the system size.

More interesting are systems that show Hilbert space fragmentation (HSF)²⁰, which we will focus on in this paper. In these systems, the Hamiltonian takes a block-diagonal form in a basis given by a product of local states, and the total number of blocks increases exponentially with the size of the system. This differs from what occurs when there are a finite number of global symmetries; if there is a finite number r of conserved quantities in the system, the number of blocks grows polynomially as V^r , where V is the volume of the system. We emphasize that if there is HSF, the ETH fails in general with respect to the total Hilbert space. Another striking feature is the presence of frozen states which are basis vectors that are eigenstates of the Hamiltonian with zero energy. The number of such frozen states grows exponentially with the system size. The most interesting kind of HSF is strong fragmentation, where the size of the largest fragment is exponentially smaller than the full many-body Hilbert space.

There are some challenges in understanding different aspects of fragmented systems where the constants of motion cannot be expressed as integrals of local observables. Some important steps towards a complete characterization are the concepts of “statistically localized integrals of motion”²¹ (which is equivalent to our construction of IS), commutant algebras²², and the algebra of matrix product operators²³; these uniquely label the disconnected subspaces in several fragmented systems. Moreover, the construction of commutant algebras further categorizes this mechanism based on the basis states in which fragmentation takes place. If the fragmentation occurs in a particle number basis, it is called classical fragmentation^{24,25}, whereas fragmentation happening in an entan-

*This author contributed to Sections I-III and Appendices A-C.

gled basis is dubbed as secondary fragmentation²⁶ or quantum fragmentation^{22,27}. The model studied in our paper will turn out to show classical fragmentation.

Examples of such systems for which the strong ETH is not valid are systems with dipole conservation or conserved magnetization^{20,23–25,28–31}. In these systems, HSF occurs due to strong constraints on the mobility of excitations. However, there are also examples of HSF which do not involve dipole conservation^{26,27,32–37}. There are also some studies of periodically driven models where HSF has been found recently^{38–40}.

In this work, we introduce and study a one-dimensional correlated-hopping model of spinless fermions with terms informing four consecutive sites. Using a bond-site mapping to a dual lattice^{30,31}, this model can be mapped to an assisted pair-flipping model that only has terms involving three sites. We find that this system shows strong HSF.

To characterize the HSF in this system, we use the idea of “irreducible strings” (IS). The concept of IS was introduced several years ago to understand exponential fragmentation (called “many-sector decomposition” at that time) in several classical models such as a deposition-evaporation model of k -mers^{41,42} and a diffusing dimer model⁴³. Recently, the idea of IS has been rediscovered and called ‘statistically localized integrals of motion’. In particular, Rakovszky et al²¹ have used the idea of statistically localized integrals of motion to study various systems exhibiting strong HSF, and they have also shown that correlation functions have a non-uniform profile whose value near the boundary does not agree with the microcanonical expectation value.

Remarkably, many features of our model can be understood in terms of IS, such as the total number of fragments and total s number of frozen states. We compute the size of the largest fragment employing the idea of IS and an enumerative combinatorics of characters^{41–44}, which we have verified by direct numerical checks. We find that strong ETH is not satisfied in our model, as suggested by an analysis of the energy level spacing ratio^{10,45,46} and expectation values of few-body operators of all the eigenstates (without resolving into fragments), which is always the case for a typical fragmented system²⁵. A similar analysis for the largest fragment indicates that this subspace is non-integrable. We provide evidence that a weaker form of subspace-restricted ETH still holds within sufficiently large fragments which we call typical fragments^{22,24}.

Next, we study the out-of-equilibrium dynamics in our model to look for dynamical signatures of the lack of thermalization. We find that infinite-temperature autocorrelation functions starting from a random initial state in the full Hilbert space also show that strong ETH is not satisfied. Moreover, the boundary autocorrelation function oscillates around a finite saturation value at long times, which is much larger than the bulk saturation value^{21,22,25}. We provide an understanding of the non-uniform profiles of the bulk and boundary spectra by computing the lower bound of these two autocorrelation functions using the Mazur inequality^{47,48} and a knowledge of the fragmentation structure of the model. We also study the entanglement dynamics in the largest fragment. This confirms our previous finding that ETH is not satisfied in the full Hilbert space, but a weak subspace-restricted ETH is valid within the

largest fragment.

We conclude by presenting an experimentally realizable $t - V$ model with a spatial periodicity of four which can generate our correlated-hopping model in a particular limit. Another way to realize our model is through a periodically driven system with an on-site potential with a spatial periodicity of four sites. We find that for some particular driving parameters, an interplay between dynamical localization (i.e., the effective hopping becoming zero as a result of the driving), resonances between different states, and density-density interactions gives rise to precisely this model³⁹.

The plan of this paper is as follows. In Sec. II, we discuss the Hamiltonian of our model, its global symmetries, and a mapping to a model with three-site terms. In Sec. III, we consider the three-site form of the model, and we discuss the fragmentation of the Fock space, the number of fragments, the number of frozen fragments which contain only one state each, and a description of some special fragments, including the largest sector. Some details are relegated to the Appendices. In Secs. IV–VII, we consider the four-site form of the model. In Sec. IV, we provide evidence for ergodicity breaking and non-integrability through the expectation values of some local operators, the half-chain entanglement entropy, and the distribution of the energy level spacing. In Sec. V, we study dynamical signatures of HSF by looking at the long-time behavior of autocorrelation functions and the time evolution of the half-chain entanglement entropy. In Sec. VI, we discuss how our model may arise in the large-interaction limit of a variant of the $t - V$ model in which nearest-neighbor interactions have a period-four structure. For the purposes of comparison, we discuss in Sec. VII a different model with four-site terms which has been studied extensively in recent years as an example of a system exhibiting HSF. We show that this can be mapped to a model with three-site terms which describes stochastic evolution of diffusing dimers on a line. The complete structure of the HSF in the latter model was found exactly many years ago using the idea of IS⁴³. We summarize our results and point out some directions for future studies in Sec. VIII.

II. MODEL HAMILTONIAN AND SYMMETRIES

We consider a one-dimensional spinless fermionic model which, for an infinitely large system, is described by the Hamiltonian

$$H_1 = \sum_j (n_j - n_{j+3})^2 (c_{j+1}^\dagger c_{j+2} + c_{j+2}^\dagger c_{j+1}). \quad (1)$$

Here c_j (c_j^\dagger) is a fermionic annihilation (creation) operator on site j , and $n_j = c_j^\dagger c_j$ can take values 0 or 1. This Hamiltonian connects the following pairs of states involving four consecutive sites,

$$\begin{aligned} 1100 &\leftrightarrow 1010 \\ 0101 &\leftrightarrow 0011. \end{aligned} \quad (2)$$

We define a spin variable $Z_j = 2n_j - 1$ which can only take the values ± 1 at site j . Apart from translation and inversion symmetries, this model has three additional global symmetries: total particle number C_1 , and two staggered quantities C_2 and C_3 given by

$$\begin{aligned} C_1 &= \sum_j n_j, \\ C_2 &= \sum_j (-1)^j Z_{2j} Z_{2j+1}, \\ C_3 &= \sum_j (-1)^j Z_{2j-1} Z_{2j}. \end{aligned} \quad (3)$$

Moreover, at half-filling, this model is invariant under a modified particle-hole transformation given by $c_j \leftrightarrow (-1)^j c_j^\dagger$. It turns out that these are only three of many other conserved quantities which can be characterized in terms of a construct called irreducible strings; this will be discussed in Sec. III.

The energy spectrum of this model has an $E \rightarrow -E$ symmetry. This can be seen by noting that the transformation $c_j \rightarrow (-1)^j c_j$ and $c_j^\dagger \rightarrow (-1)^j c_j^\dagger$ changes the Hamiltonian $H \rightarrow -H$.

The model in Eq. (1) can be mapped to a different model with a Hamiltonian in which the degrees of freedom lie on the bonds of the original lattice, and the new Hamiltonian is a sum of terms involving only three consecutive sites; this makes it easier to study the system. We map states for a bond $(j, j+1)$ to a state on the site $j+1/2$ on the dual lattice following the rules,

$$\begin{aligned} |01\rangle &\rightarrow |1\rangle, & |10\rangle &\rightarrow |1\rangle, \\ |00\rangle &\rightarrow |0\rangle, & |11\rangle &\rightarrow |0\rangle. \end{aligned} \quad (4)$$

This is clearly a two-to-one mapping from the four-site model to the three-site mode on the dual lattice. For example, the two states 10101010 and 01010101 of the four-site model (these states are related to each other by a particle-hole transformation) map to a single state 1111111 of the three-site model.

We see that the three-site model has two states 0 and 1 at each site, and Eq. (2) implies that only the following transitions are allowed for this model,

$$111 \leftrightarrow 010. \quad (5)$$

The model is therefore described by a Hamiltonian which involves only three consecutive sites of the dual lattice,

$$H_2 = \sum_j n_{j+1} (d_j^\dagger d_{j+2}^\dagger + d_{j+2} d_j), \quad (6)$$

where $n_j = d_j^\dagger d_j$. This rule implies that a pair of spinless fermions can be created or annihilated on two next-nearest-neighbor sites provided that the site in the middle is occupied. It is important to note that this three-site Hamiltonian does not conserve the total particle number unlike the four-site model. A summary of the original and final Hamiltonians in Eqs. (1) and (6) and the bond-site mapping connecting the

two is shown in Fig. 1.

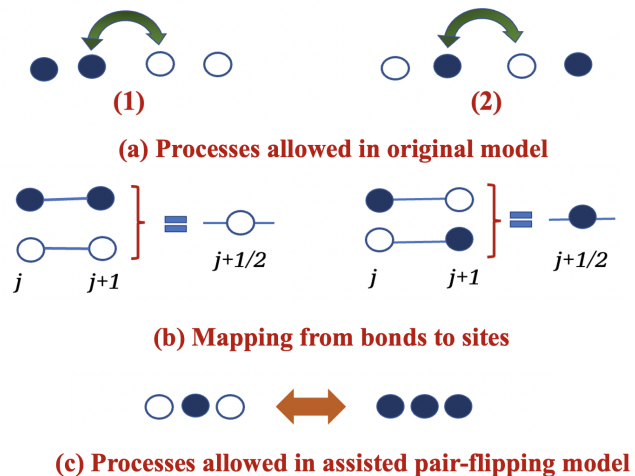


FIG. 1: (a) Processes allowed in original correlated-hopping model with terms involving four consecutive sites. (b) Mapping of bonds to sites. (c) The bond-site mapping converts the correlated-hopping model to an assisted pair-flipping model with terms involving three consecutive sites. Here filled and empty circles represent occupied and unoccupied sites respectively.

III. FRAGMENTATION OF THE HILBERT SPACE

In this section, we will show how kinetic constraints in our model shatters the Hilbert space leading to an exponentially large number of fragments in the local number basis. The fragmentation structure can appear in a variety of forms, such as frozen fragments consisting of a single eigenstate of the Hamiltonian and fragments with a finite or exponentially large number of states.

A. Irreducible strings

We first discuss the fragmentation structure in the three-site model which allows the transition described in Eq. (5); the analytical treatment is much simpler in the three-site language. It is convenient to define a Hamiltonian which only has matrix elements between the states 010 and 111. We therefore define Pauli matrices σ_j^α at site j (where $\alpha = x, y, z$), so that states 1 and 0 at site j corresponds to $\sigma_j^z = \pm 1$. In terms of these Pauli spin operators, the Hamiltonian becomes

$$H_3 = \sum_j (\sigma_{j-1}^+ \sigma_{j+1}^+ + \sigma_{j-1}^- \sigma_{j+1}^-) \left(\frac{1 + \sigma_j^z}{2} \right). \quad (7)$$

Note that this expression differs from H_2 in that it is defined in terms of Pauli spin operators which commute at different sites. This is an assisted spin-flipping Hamiltonian in which a pair of spins can flip on next-nearest-neighbor sites provided the site in the middle has spin \uparrow . The number of states in a system

with L sites is 2^L . We will consider open boundary conditions (OBC) to perform our analysis of fragmentation. One should note that the transition rules shown in Eq. (7) imply that

$$11110 \leftrightarrow 01010 \leftrightarrow 01111. \quad (8)$$

This implies that a string of four 1's can move across either a 0 or a 1 (trivially). This will be important later to understand different features of the HSF occurring in this model.

We will show below that the model in Eq. (7) has an exponentially large number of fragments. These fragments are most easily characterized in terms of a construction called IS which act as an exponentially large number of conserved quantities. This construction of IS is a variation of the construction used earlier in Refs. 41–43. This is defined as follows.

A basis configuration is characterized by a binary string of length L , e.g., 0011010 \dots . We read the string from left to right, move the first occurrence of 1111 to the left end of the string and then delete it. This reduces the length of the string by 4. We repeat this till no further reduction is possible. Then, we read the remaining string from left to right, and change the first occurrence of 010 to 111. If this generates a 1111, we move it to the leftmost end and delete this to get a string of reduced length. The steps $1111 \rightarrow \phi$ (null string), and $010 \rightarrow 111$ are repeated, till no further change can be made. The final string is the IS corresponding to the initial string. As an example, one can see that the IS for the string configuration 01111010101 reduces to 001 by the rules mentioned above; this is depicted in Fig. 2.

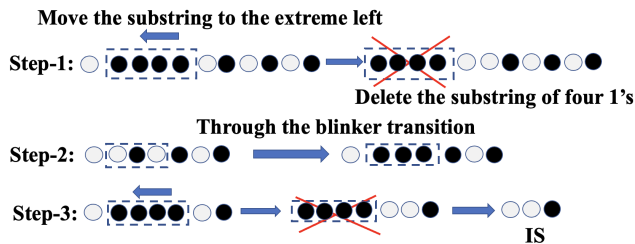


FIG. 2: Illustration of IS construction for a given binary string configuration.

The usefulness of the IS construction comes from the observation that two states belong to the same fragment if and only if they have the same IS. To prove this assertion, we note that the strings 01111 and 11110 are obtainable from each other as shown in Eq. (8). Hence one may treat a group of four adjacent 1's as a block that can slide across a 0, and it can slide across a 1 trivially. Thus, we can push any such blocks of 1111 to the left end of the system and delete them.

An IS of length $L - 4r$ corresponds to a root state of length L which has $4r$ 1's at the left. We also note that for each of the steps going from the initial string to the root state, the inverse steps are also allowed through the transitions $010 \leftrightarrow 111$. Hence, if two configurations have the same root state, they can be reached from each other. The Hilbert space fragment corresponding to a given IS is spanned by all the configura-

tions that have that IS. Thus the IS acts as a unique label for the fragment.

B. Determining the number of fragments

To calculate the number of fragments, it is convenient to define a number $M(n)$ which is the number of distinct IS of length n . We know that an IS cannot contain the substrings 010 or 1111 anywhere. Using this fact, we can calculate $M(n)$, for $n > 3$, using a transfer matrix method as shown in Appendix A.

n	0	1	2	3	4	5	6	7	8	9	10	11	12
$M(n)$	1	2	4	7	11	18	29	47	76	123	199	322	521

TABLE I: Values of $M(n)$ versus n .

It is convenient to define $M(0) = 1$. Clearly, $M(1) = 2$, $M(2) = 4$ and $M(3) = 7$. The results for the first few values of M are given in Table I. Given $M(n)$, the number of fragments of length L with OBC is given by

$$N_{OBC}(L) = \sum_{r=0}^{\lfloor L/4 \rfloor} M(L - 4r), \text{ for } L > 4. \quad (9)$$

The resulting values are used to analytically calculate the $N_{OBC}(L)$, given in Table II; we have verified these values numerically. We also list the corresponding values for PBC found numerically (using a method described in Appendix A). We find that both N_{OBC} and N_{PBC} grow asymptotically as τ^L , where $\tau = (\sqrt{5} + 1)/2 \simeq 1.618$ is the golden ratio.

L	4	5	6	7	8	9	10	11	12
N_{OBC}	12	20	33	54	88	143	232	376	609
N_{PBC}	10	13	20	32	59	81	131	207	363

TABLE II: Values of N_{OBC} and N_{PBC} versus L obtained by numerical enumeration.

C. Description of frozen fragments

The model contains an exponentially large number of eigenstates that do not participate in the dynamics; we call these ‘‘frozen’’ states. The frozen states $|f_j\rangle$ are all product states in the particle number basis, and are annihilated by the Hamiltonian so that $H|f_j\rangle = 0$. Hence these states are zero-energy eigenstates of the model Hamiltonian. Two trivial examples of such states in the four-site language are fully empty and fully occupied states in the particle number basis, i.e., $|\dots 0000 \dots\rangle$ and $|\dots 1111 \dots\rangle$, respectively.

In a frozen state, there cannot be any occurrence of substrings 010 or 111, and the length of the IS must be L . It is then straightforward to set up a transfer matrix to determine the exact numbers of such states $N^{frozen}(L)$ for a system of size L . The details of the calculation are given in Appendix B. We find that the number of frozen fragments for a system of size L grows as 1.466^L for large L . For the first few values of L , the number of frozen states $N^{frozen}(L)$ is shown in Table III for both OBC and PBC.

L	3	4	5	6	7	8	9	10	11	12
N_{OBC}^{frozen}	6	9	13	19	28	41	60	88	129	189
N_{PBC}^{frozen}	4	5	6	10	15	21	31	46	67	98

TABLE III: N_{OBC}^{frozen} and N_{PBC}^{frozen} versus L with OBC and PBC respectively.

We note here that the frozen states possess many of the features of quantum many-body scars. They have exactly zero energy (and hence lie in the middle of the energy spectrum), and this does not change if the coefficients of the terms in the Hamiltonian in Eq. (1) are taken to be random numbers instead of all being set equal to 1. Further, since the frozen states are all product states in real space, they trivially have zero entanglement entropy between any two parts of a system with either OBC or PBC.

D. Description of some simple integrable fragments

We will now present some examples of fragments which consist of more than one state (and are therefore not frozen) but in which the Hamiltonian dynamics is integrable.

The first example of an integrable fragment is a set of multiple "blinkers" each of which flips back and forth between two states. For example, we can have an IS of the form

$$\dots 00011100111000 \dots$$

These fragments consist of a sea of 0's with islands of three consecutive sites that can flip between 010 and 111 but are fully localized in space. The general state in such a fragment can be obtained by concatenating the substrings 0, 1110 and 0100. For a system with OBC, the number of states in the fragment can be found by defining a transfer matrix T following a procedure similar to the one given in Appendix A. We find that T is a 8×8 matrix whose characteristic polynomial is given by $\lambda^5(\lambda^3 - \lambda^2 - 1)$. The largest root of this equation is approximately 1.466 (see Eqs. (B2) and (B3)), and the number of states therefore grows with system size as 1.466^L asymptoti-

cally. For each blinker, labeled by an integer $j = 1, 2, \dots, r$, we can introduce a Pauli matrix τ_j^z which is equal to ± 1 for 111 and 010 respectively. The number of states in this fragment is equal to 2^r , and the effective Hamiltonian is given by $H_{eff} = \sum_{j=1}^r \tau_j^x$. It is then easily seen that the energy eigenvalues for this fragment are given by $\sum_{j=1}^r e_j$, where each e_j can take values ± 1 .

The second example we consider is a fragment whose IS is made of $L - 4$ 0's. The configuration will have a single substring 1111 or a single substring 101 in a sea of zeroes; the total number of such states is $2L - 5$. We can think of these as the states of a particle which can be either in a state $a_{j+3/2} = 1111$ at sites $(j, j+1, j+2, j+3)$, where $j = 1, 2, \dots, L-3$, or in a state $b_j = 101$ at sites $(j-1, j, j+1)$, where $j = 2, L-1$. The Hamiltonian can take the state $|a_{j+3/2}\rangle$ to either $|b_{j+1}\rangle$ or $|b_{j+2}\rangle$. This gives us a tight-binding model of a particle that moves on a finite line with $2L - 5$ sites. We then find that the energy levels of this effective Hamiltonian are

$$E_k = 2 \cos[\pi k / (2L - 4)], \text{ where } k = 1, \dots, 2L - 5. \quad (10)$$

E. Description of the largest fragment

We now consider the largest fragment, which includes all the states reachable from the configuration of all 1's. The corresponding IS reduces to one of the four possibilities ϕ (null string) or 1 or 11 or 111. Let D_L denote the size of the fragment corresponding to the IS given by $111 \dots 111$, i.e., 1 repeated L times. We will compute the generating function

$$V(x) = \sum_{L=0}^{\infty} D_L x^L. \quad (11)$$

Following a lengthy calculation whose details are shown in Appendix C, we obtain the expression

$$V(x) = \frac{1}{1 - x - \left(\frac{1 - \sqrt{1 - 12x^4}}{6x} \right)}. \quad (12)$$

Writing this in the form given in Eq. (11), we find that the growth of D_L for large L is determined by the singularities of $V(x)$ lying closest to the origin⁴¹⁻⁴³. According to Eq. (12), these singularities lie at $x_0^4 = 1/12$, namely, the fourth roots of $1/12$. Hence D_L grows as $(1/|x_0|)^L$, i.e., 1.8612^L for large L . To confirm this, we Taylor expand Eq. (12) which generates the series

$$\begin{aligned}
V(x) = & 1 + x + x^2 + 2x^3 + 3x^4 + 4x^5 + 6x^6 + 12x^7 + 19x^8 + 28x^9 + 46x^{10} + 92x^{11} + 150x^{12} + 232x^{13} + 396x^{14} \\
& + 792x^{15} + 1315x^{16} + 2092x^{17} + 3646x^{18} + 7292x^{19} + 12258x^{20} + 19864x^{21} + 35076x^{22} + 70152x^{23} + \dots,
\end{aligned}
\tag{13}$$

We have checked that these numbers perfectly agree with those obtained by brute force numerical enumeration. We note that the exponential growth rate of the largest sector with L is slower than the total number of states 2^L , and goes to zero in the limit of large L , which establishes the strong fragmentation²⁵ of the Hilbert space in this model.

F. Typical and atypical fragments

Having discussed the idea of IS and seen several examples of fragments, it is useful to discuss *typical* and *atypical* fragments. It is difficult to differentiate between the two very precisely but we may proceed roughly as follows.

We first show the distribution of fragment numbers for different system sizes with OBC in Fig. 3. A fragment size equal to 1 (left edge of the figure) corresponds to frozen fragments which are discussed in Sec. III C. The largest fragment (right edge of the figure) will be discussed in Sec. III E.

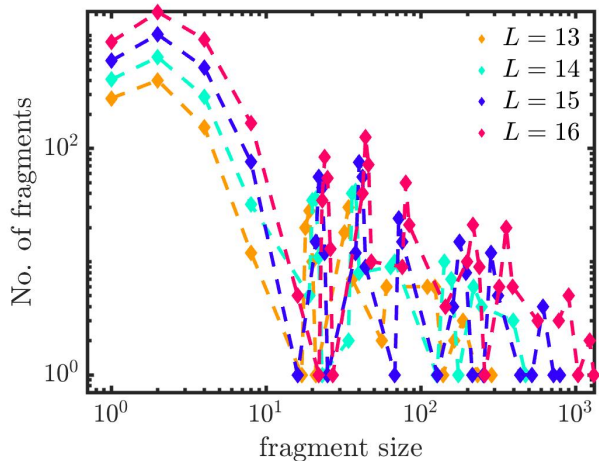


FIG. 3: Plot showing the distribution of number of fragments versus sizes of fragments for four different system sizes, $L = 13, 14, 15$ and 16 , with OBC.

We can qualitatively estimate the average size of a fragment as follows. While the dimension of the total Hilbert space is 2^L , we saw earlier that the number of fragments grows asymptotically as τ^L . We may therefore expect a typical fragment to have a size of the order of $(2/\tau)^L \simeq 1.236^L$. For $L = 13, 14, 15$ and 16 , this goes from about 16 to 30. Indeed we see that $16 - 30$ lies near the middle of the ranges of fragment sizes shown in Fig. 3.

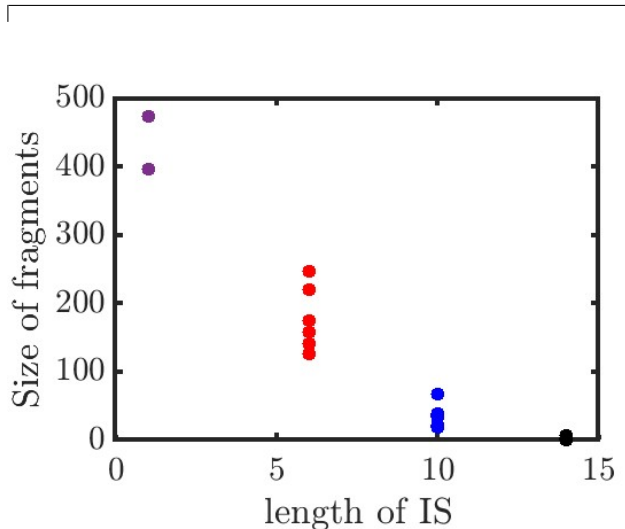


FIG. 4: Plot of the sizes of fragments versus the lengths of their IS for $L = 14$ with OBC.

Next, we examine numerically if there is any relation between the size of a fragment and the length of its IS. This is shown in Fig. 4 for $L = 14$, and we observe that the two quantities appear to be inversely related. (Note that the IS lengths can only be equal to $L, L - 4, L - 8, L - 12, \dots$). We see from the figure that two fragments with the same IS lengths may have different sizes, but the ratio of their sizes is of order 1. Frozen fragments have only one state each and the length of their IS is equal to L ; hence they correspond to the point at the bottom right of Fig. 4.

We may now define an atypical fragment as one which has an exponentially large number of states (in the limit $L \rightarrow \infty$), and whose IS has a length l where $L - l \ll L$. With this definition, both frozen fragments (which have $l = L$) and the simple integrable fragments discussed in Sec. III D are atypical. On the other hand, the largest fragment and other fragments with short IS are all typical. The significance of a typical fragment is that it is expected to behave like a standard macroscopic ensemble, and we may expect a weak version of ETH to hold within it.

We have found numerically that the ground state and low-lying excited states generally lie in the largest fragment and other fragments which have comparable numbers of states. Thus the low-energy properties of this model are dominated by the largest fragments.

IV. SUBSPACE-RESTRICTED ETH IN SYSTEMS WITH STRONG HILBERT SPACE FRAGMENTATION

The existence of atypical fragments, like the frozen states and integrable fragments (for example, fragments with n blinkers), implies that strong ETH is not satisfied with respect to the full Hilbert space in our model. This motivates us to modify the ETH as follows. Suppose that a Hamiltonian in a basis given by products of local states has a fragmented structure, such that energy eigenstates have non-zero components only within a single fragment. Then it seems natural to postulate that in each fragment, correlation functions of local observables calculated in the eigenstates of the Hamiltonian will tend to values corresponding to a restricted microcanonical ensemble, in which all the the eigenstates (except for a set of measure zero) having a given energy density are equally likely. We will call this a weak subspace-restricted ETH. In our model, this should be satisfied in all the typical fragments but it need not be satisfied in atypical fragments.

We will now check the validity of a weak version of ETH within the largest fragment, as well as the validity of ETH in other sectors in the full Hilbert space at half-filling for the four-site model. We first examine the variation of expectation values of local observables for all eigenstates of the Hamiltonian and the variation of the half-chain entanglement entropy $S_{L/2}$ as a function of the energy E without resolving the fragmentation structure. In Figs. 5 (a) and (b), we show the expectation values of the local observables $\langle n_{L/2} \rangle$ and $\langle n_{L/2+1} n_{L/2} \rangle$ as a function of the energy density E/L for all the eigenstates for three different system sizes, $L = 12, 14$ and 16 . We see that the widths of the distributions do not decrease significantly with increasing system sizes. Moreover, we also analyze the standard deviations of the differences of $\langle E|A|E \rangle - \langle A \rangle_E$, where $|E \rangle$ denotes an eigenstate of the Hamiltonian at energy E , and $\langle A \rangle_E$ is the microcanonical expectation value of A at energy E obtained by averaging over eigenstates within an energy window $\Delta E/L = 0.025$ ⁴⁹. For our case, we consider A to be $n_{L/2}$ and $n_{L/2+1} n_{L/2}$, and then examine the standard deviation σ_A as a function of the total Hilbert space dimension D at half-filling, as shown in Figs. 5 (c) and (d). In both cases, we observe that the values of σ_A do not change notably with increasing values of D . This confirms that the strong version of diagonal ETH is not valid in our model within the full Hilbert space at half-filling. A similar behavior was seen earlier in other models showing HSF ^{1,2}.

Next, we discuss the spectrum of the half-chain entanglement entropy $S_{L/2}$ as a function of the energy E for the full Hilbert space (without resolving the individual fragment) at half-filling with OBC for three different system sizes, $L = 14, 16$ and 18 . This is shown in Figs. 6 (a-c). In all three figures, we see that many low-entanglement states are present in the middle of the spectrum. Further, the values of entanglement entropies for all the eigenstates are much smaller than the thermal value $S_{page} = (L \ln 2 - 1)/2$ ⁵⁰ shown by the dash-dot lines; this again shows that ETH with respect to the full Hilbert space is not satisfied. Moreover, the entropies of the eigenstates do not lie within a narrow band when plotted

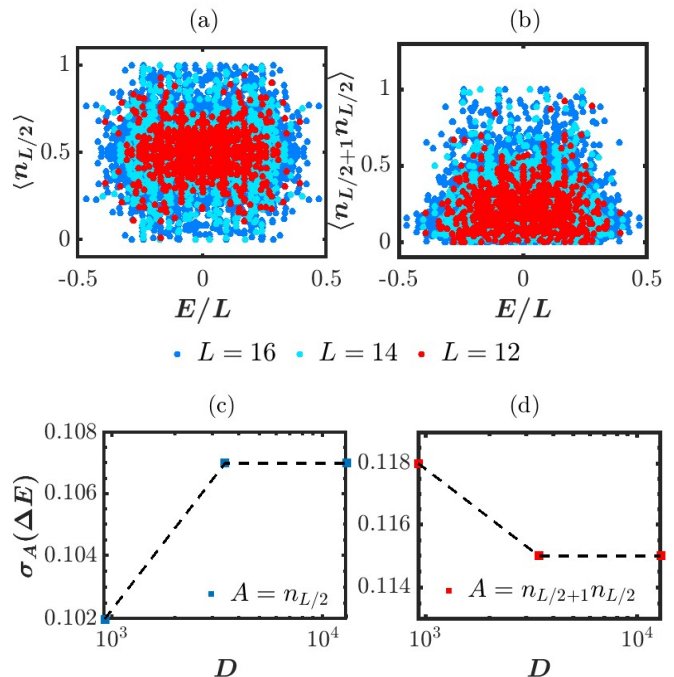


FIG. 5: Scatter plots of (a) $\langle n_{L/2} \rangle$ and (b) $\langle n_{L/2+1} n_{L/2} \rangle$ for all the eigenstates as a function of energy density E/L for different distribution sizes, $L = 12, 14$ and 16 . In all three cases, the widths of the distribution do not appear to decrease significantly with increasing L . The standard deviation σ_A of $\langle n_{L/2} \rangle$ and $\langle n_{L/2+1} n_{L/2} \rangle$ as a function of Hilbert space dimension D in an energy window of $\Delta E/L = 0.025$ are shown in plots (c) and (d). The values of σ_A do not decrease significantly with increasing Hilbert space dimensions similar to Figs. (a-b); this behavior is also not consistent with strong ETH.

against the energy. Rather they are distributed over a wide range of values which are all much smaller than the thermal value; this is exactly the opposite of what is typically observed for a system obeying strong ETH. Also, the width of the entanglement entropy spectrum does not shrink with increasing L unlike a thermal system, indicating a manifestly non-thermalizing behavior as a consequence of strong HSF.

We next study the energy level spacing distribution which is often studied to probe whether a model is integrable or non-integrable^{10,45,46}. It is well-known from the theory of random matrices that non-integrable systems described by random matrices show level repulsion, but integrable models, or models with extra conserved quantities do not. To quantify the degree of level repulsion in a model, it is often better to study the level spacing ratios rather than the level spacing distribution of the sorted eigenspectrum. To do so, we define the level spacing ratios of the sorted eigenspectrum by $r_n = \delta_{n+1}/\delta_n$, where $\delta_n = E_{n+1} - E_n$ and E_n is the n -th energy eigenvalue. If a system is integrable, r follows the Poisson distribution, i.e., $P(r) = 1/(1+r)^2$, while non-integrable systems described by real Hermitian Hamiltonians follow the Gaussian orthogonal ensemble (GOE) distribution^{51,52} which is given

by the distribution

$$P(r) = \frac{27}{8} \frac{(r + r^2)}{(1 + r + r^2)^{5/2}}. \quad (14)$$

It is also convenient to study the distribution of \tilde{r} , which is defined as

$$\tilde{r}_n = \frac{\min(\delta_{n+1}, \delta_n)}{\max(\delta_{n+1}, \delta_n)} = \min(r_n, 1/r_n). \quad (15)$$

For the two classes mentioned above, the distribution of \tilde{r} follows $P(\tilde{r}) = 2P(r)\theta(1-r)$, where $\langle \tilde{r} \rangle = 0.386$ for Poisson and 0.536 for GOE.

To numerically compute the level spacing statistics of the consecutive energy levels for the sorted spectrum of the full system, we add a small uniformly distributed random on-site potential with strength $w = 0.01$ for an 18-site system of $L = 18$ with OBC to break all the discrete symmetries and to eliminate any accidental degeneracies^{22,24,53}. We note that the presence of an on-site disorder preserves the fragmentation structure of the full Hilbert space. In addition, we also impose the half-filling condition to choose a particular C_1 symmetry sector, but we do not restrict the analysis within particular C_2 and C_3 symmetry fragments since these two global symmetries are only well-defined for $L = 4n$. As shown in Fig. 6 (d), we see that the distribution of \tilde{r} , called $P(\tilde{r})$, is indistinguishable from a Poisson curve with $\langle \tilde{r} \rangle \simeq 0.383$; this is very close to the value observed for an integrable system. The exponentially large number of dynamically disconnected fragments act as large number of conserved quantum numbers that forbid level repulsion as in an integrable system^{53,54}.

Finally, we study the behavior of the largest fragment generated by enumerating the root state $1010 \dots 1010$ for the original model with terms involving four consecutive sites for $L = 22$ with OBC (the size of this fragment is 19864). In the three-site model, this state reduces to the state $111 \dots 111$, which generates the largest fragment. In Fig. 7 (a), we show the entanglement entropy as a function of E for the largest fragment. We see that the entropies of most of the eigenstates fall on a curve, with a small number of outlying low-entanglement eigenstates in the middle of the spectrum. In Fig. 7 (b), we perform the same analysis with a small uniformly distributed random on-site disorder with strength $w = 0.01$ to discard any discrete symmetries and to avoid any accidental degeneracies^{22,24}. (The random on-site disorder preserves the fragment structure). We see that the spectrum in this case shows features identical to the previous case; further, it stabilizes the low-entanglement eigenstates, as can be seen in Fig. 7 (b). We find that the consecutive energy level spacing statistics for the eigenstates within this fragment with small disorder is consistent with GOE level statistics with $\langle \tilde{r} \rangle \simeq 0.524$ which is close to the GOE value. This points towards non-integrability of the largest fragment²⁴, as shown in Fig. 7 (c).

In Figs. 8 (a) and (b), we show the average values of $n_{L/2}$ and $n_{L/2+1}n_{L/2}$ for all the eigenstates within this subspace for $L = 14, 16, 18$ and 20 where the fragment sizes are 232, 792, 2092 and 7292, respectively. We see that the width

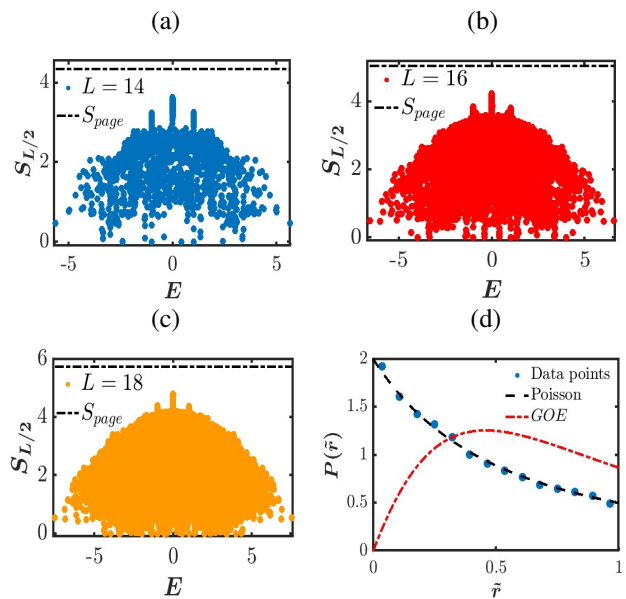


FIG. 6: (a-c) Plots showing the half-chain entanglement entropy $S_{L/2}$ versus E for the full Hilbert space at half-filling for $L = 14, 16$ and 18, respectively, with OBC. In all three cases, the entanglement entropies of all the eigenstates do not lie within a narrow band, and they have values much smaller than the thermal value shown by the dash-dot lines at the top. Also, the widths of the spectra do not decrease with increasing L , indicating that strong ETH is not valid. (d) Plot showing the probability distribution of \tilde{r} for the sorted eigen-spectrum for the full Hilbert space at half-filling for a 18-site system with OBC. (In order to break any discrete symmetries, we add a small uniformly distributed random on-site potential with strength $w = 0.01$. The disorder preserves the fragment structure of the full Hilbert space). The distribution $P(\tilde{r})$ follows a Poisson curve with $\langle \tilde{r} \rangle \simeq 0.383$.

of this distribution becomes narrower with increasing system size. We then perform the same analysis as Figs. 5 (c) and (d) within the largest fragment in Figs. 8 (c-d). We see that the standard deviations σ_A of local observables decrease with increasing values of fragment size D . Moreover, σ_A approximately scales as $1/\sqrt{D}$ with some deviation, which has been seen earlier in the ETH obeying systems⁴⁹. This behavior again indicates that the subspace-restricted diagonal ETH is satisfied within this fragment. However, there are some outlying states which do not show thermal behavior as shown in 8 (a) and (b).

We also observe numerically that the largest fragment contains a large number of states, $N_{E=0}$, with exactly zero energy. The variation of $N_{E=0}$ with the size D_L of the largest fragment (L is the system size) is presented in Table IV, and Fig. 9 shows a log-log plot of $N_{E=0}$ versus D_L . The numerical fitting indicates that $N_{E=0}$ grows as $D_L^{0.59}$. It has been shown earlier in some models^{55,56} that there are index theorems which give a lower bound on the growth of $N_{E=0}$ versus D_L . In these models, index theorems imply that $N_{E=0} \gtrsim \sqrt{D_L}$. Fig. 9 implies that such a square root bound is also satisfied by the largest fragment in our four-site model. However we have not been able to derive this bound analyti-

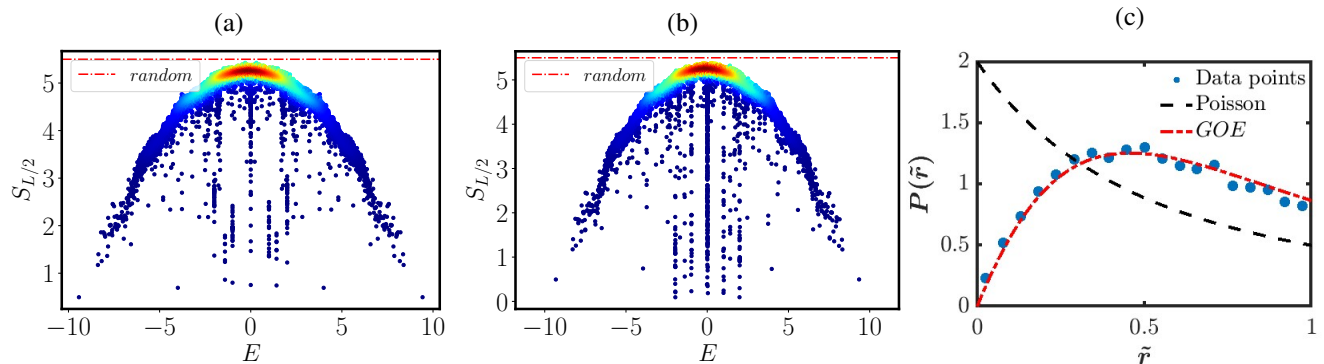


FIG. 7: (a-b) Plots showing the half-chain entanglement entropy $S_{L/2}$ versus E for the largest fragment produced by enumerating the root configuration $1010 \dots 1010$ in the four-site model for $L = 22$ (the fragment size is 19864) with OBC with (a) no disorder and (b) a small uniformly distributed disorder with strength $w = 0.01$, respectively. (a) The entropies for most of the eigenstates within this fragment lie within a narrow band, apart from some low-entanglement outlying eigenstates in the middle of the spectrum. (b) The spectrum in the presence of disorder exhibits identical features. In both cases, the red dash-dot line denotes the entanglement entropy of a random state within this particular fragment. (c) Plot of the probability distribution $P(\tilde{r})$ versus \tilde{r} for case (b). $P(\tilde{r})$ obeys the GOE distribution, indicating non-integrability of this fragment.

cally due to the lack of a simple structure of the states and of the Hamiltonian within this fragment. Finally, we note that the square root bound also holds for the full Hilbert space. This is because the frozen states are trivially zero-energy eigenstates of the Hamiltonian, and we saw in Sec. III C that the number of such states grows asymptotically as 1.466^L . This is much larger than a square root bound since $\sqrt{2^L} \simeq 1.414^L$.

We thus see that the largest fragment contains a large number of zero energy states, and many of these have an anomalously low entanglement entropy as shown in Fig. 7 (a). The presence of these exceptional states implies that the subspace-restricted ETH is satisfied with the largest fragment in a weaker sense.

L	D_L	$N_{E=0}$
6	4	2
8	12	2
10	28	6
12	92	6
14	232	22
16	792	24
18	2092	80
20	7292	90
22	19864	308

TABLE IV: Table showing the system size L , the size D_L of the largest fragment generated from the root state $1010 \dots 1010$ in the four-site model, and the number of zero energy states $N_{E=0}$ in this fragment.

In Figs. 10 (a-b), we study the thermal behavior of eigenstates within a fragment generated from a randomly chosen root state 10100010010010101010 for $L = 20$ in the four-site model; this fragment has dimension $D = 574$. This root state reduces to 11100110110111111111 due to bond-site mapping,

whose IS, 11100110110 has a length $(L + 3)/2$ in the three-site model, unlike the largest fragment which has the shortest IS. In Fig. 10 (a), we show the expectation values of two local observables $n_{L/2}$ and $n_{L/2+1}n_{L/2}$ for all eigenstates within this fragment. In Fig. 10 (b), we show the difference between the expectation values of the same two observables $\langle E|A|E \rangle$ for an eigenstate at energy E from their microcanonical expectation value $\langle A \rangle_E$ obtained by averaging over eigenstates within an energy window $\Delta E = 0.025$ about E . Moreover, we consider one-fifth of the total eigenstates with energies lying in the middle of the spectrum while doing this analysis. As this difference is centered around zero, it implies that each eigenstate satisfies diagonal ETH within this fragment. One can therefore conclude that all typical fragments satisfy subsector-restricted thermalization in our model in the thermodynamic limit.

Despite the fact that ETH is not valid with respect to the full Hilbert space as shown in Figs. 5 and 6, expectation values of local observables of eigenstates within sufficiently large fragments still satisfy ETH as we see in Figs. 7 and 8. Therefore, sufficiently large fragments still satisfy ETH even in the case of strongly fragmented systems. This is also dubbed as Krylov-restricted thermalization in the literature^{20,24,37}. This kind of restricted thermalization has a significant impact on the dynamics of the system, in particular, an atypical dynamical behavior of correlation functions, which we will discuss in the next section.

V. DYNAMICAL SIGNATURES OF HILBERT SPACE FRAGMENTATION

In this section, we will study autocorrelation functions of the fermion number at different sites of the four-site model. We will see that these provide dynamical signatures of the absence of thermalization due to HSF.

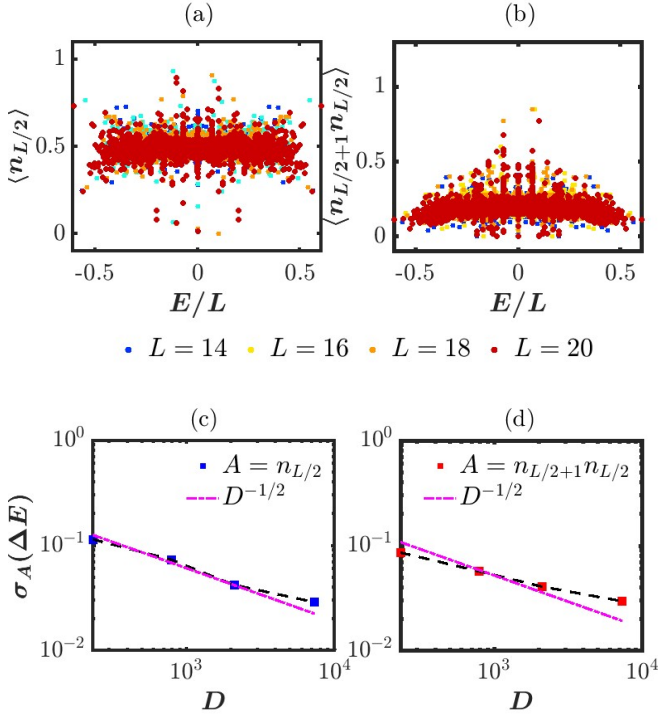


FIG. 8: Plots of (a) $\langle n_{L/2} \rangle$ and (b) $\langle n_{L/2+1} n_{L/2} \rangle$ for all the eigenstates within the largest fragment of the full Hilbert space. Most of the eigenstates within this fragment show a thermal behavior. In both cases, the bulk of the distribution becomes narrower with increasing L , but with some outlying states which do not fit within a narrow window of values of $\langle n_{L/2} \rangle$ and $\langle n_{L/2+1} n_{L/2} \rangle$. The standard deviations σ_A of $\langle n_{L/2} \rangle$ and $\langle n_{L/2+1} n_{L/2} \rangle$ as a function of the size D of the largest fragment within an energy window of $\Delta E/L = 0.025$ are shown in plots (c) and (d). We see that the values of σ_A decrease with increasing sizes of largest fragment, which approximately scale as $1/\sqrt{D}$ with a slight deviation. The decreasing values of σ_A with increasing fragment size supports the subspace-restricted ETH within the largest fragment.

A. Long-time behavior of autocorrelation functions

As a signature of the lack of thermalization due to strong HSF, we first investigate the behavior of the time-dependent correlation function

$$C_j(t) = \langle \psi | (n_j(t) - 1/2)(n_j(0) - 1/2) | \psi \rangle,$$

where n_j is the fermion number operator at site j , $|\psi\rangle$ being a typical random initial state in the full Hilbert space, which is chosen to have the form $|\psi\rangle = \sum_j a_j |f_j\rangle$ with $\sum_j |a_j|^2 = 1$, where the a_j 's are random numbers and $|f_j\rangle$ denote Fock space basis states. We will consider the case of half-filling and open boundary conditions.

In thermal equilibrium, the autocorrelation function is expected to decay to zero as $1/L$ for a system of length L . In Fig. 11 (a), we study the boundary autocorrelator, $C_1(t)$ for a

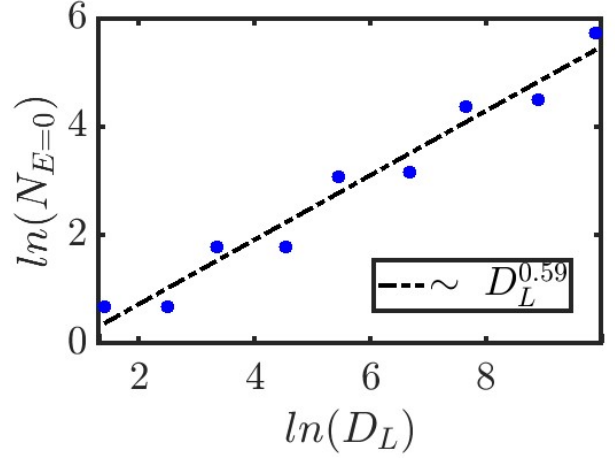


FIG. 9: Log-log plot of the number of zero energy states $N_{E=0}$ versus the size D_L of the largest fragment for system size L . The numerical fitting shows that $N_{E=0}$ grows as $D_L^{0.59}$.

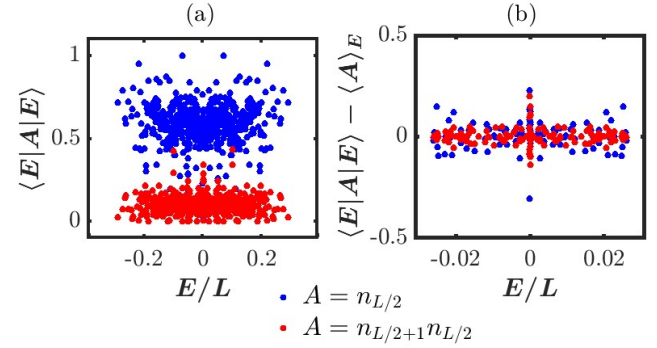


FIG. 10: (a) Expectation values of two few-body observables $A = n_{L/2}$ and $n_{L/2+1} n_{L/2}$ for all the eigenstates within the fragment generated from a root state 101000100100101010 for $L = 20$ in the four-site model. (b) Plot showing the difference between the expectation values of the observables for an eigenstate at energy E and their microcanonical value obtained by averaging over eigenstates within an energy window of $\Delta E = 0.025$. The analysis shown in Fig. (b) has been performed for one-fifth of the eigenstates in the middle of the spectrum.

system size $L = 18$ with OBC at half-filling for a random initial state in the Hilbert space. We find persistent oscillations around a finite saturation value of about 0.115 (shown in the inset of the plot) up to a long time $t \sim 10^3$. We then study the same function in the middle of the system, $C_{L/2}(t)$, for the same system size in Fig. 11 (b). We observe that $C_{L/2}(t)$ saturates to a much smaller value of about 0.045 (shown inset of the plot) at long times. In a similar manner, we show the same quantities for $L = 20$ in Fig. 11 (c-d). We see that the behaviors of $C_1(t)$ and $C_{L/2}(t)$, including the period of oscillations, do not significantly change with increasing system size. However, both quantities oscillate around finite saturation values given by 0.113 and 0.04, respectively (shown in the insets of the plots), which are slightly smaller compared to

Figs. 11 (a) and (b), respectively. We therefore conclude that the boundary correlator behaves in a different manner from the bulk correlator.

Further, strong HSF leads to a non-uniform profile of correlation function near the edge of the chain in our model model as was observed earlier in this context for other models^{21,22,25}. We examine the robustness of this non-uniform profile near the edge against perturbations by including two types of terms in the four-site Hamiltonian. The first one is a uniformly distributed random on-site potential of strength $w = 0.1$, and the results are shown in Figs. 12 (a) and (c). The second one involves the Hamiltonian

$$H' = \sum_j [(n_{j-1} - n_{j+2})^2 - \epsilon] (c_j^\dagger c_{j+1} + c_{j+1}^\dagger c_j) \quad (16)$$

where $\epsilon = 0.1$, giving the results shown in Figs. 12 (b) and (d). The first one breaks all the discrete symmetries present in the four-site model, but it preserves the fragmentation structure of the full Hilbert space. On the other hand, the second one preserves all the discrete symmetries but modifies the fragmentation structure of the full Hilbert space; the numbers of fragments generally decreases for this case since the ϵ terms connects certain states which are not connected otherwise. As shown in Figs. 12 (a) and (c), the long-time behaviors of C_1 and $C_{L/2}$ in the first case remains the same as in the unperturbed case, exhibiting an absence of thermalization. For the second case, both the correlators decay to zero after showing a non-trivial intermediate-time dynamics, as can be seen in Figs. 12 (b) and (d).

We will now explain the long-time saturation value of the autocorrelation functions by taking the fragmentation structure of the full Hilbert space into account. It can be shown that the equilibrium value of $C_j(t)$ predicted by the ETH hypothesis is zero for all values of j if our model thermalizes. Therefore, the nonuniform profile of autocorrelation function near the edge of the chain shown in Fig. 11 is an atypical behavior which arises as a consequence of subspace-restricted ETH due to strong HSF. This behavior can be explained with the help of the Mazur inequality⁴⁷, which applies to the long-time averages of autocorrelation functions in the context of thermalization. For quantum systems, an exact Mazur-type equality was obtained by Suzuki⁴⁸, which takes into account existence of constants of motion in the problem. In the same spirit, the value of the Mazur bound for fragmented Hilbert spaces is changed by taking into account the structures of invariant subspaces. We do this as follows.

We define P_i as the projection operator onto a particular fragment \mathcal{H}_i with size D_i . The set of projectors onto different fragments form a complete orthogonal set of conserved quantities such that $P_i P_j = \delta_{ij} P_j$. Using these, we define the long-time averaged autocorrelation functions

$$F_j = \lim_{T \rightarrow \infty} \frac{1}{T} \int_0^T dt \langle (n_j(t) - \frac{1}{2})(n_j(0) - \frac{1}{2}) \rangle,$$

where n_j is the fermion number operator at site j . These sat-

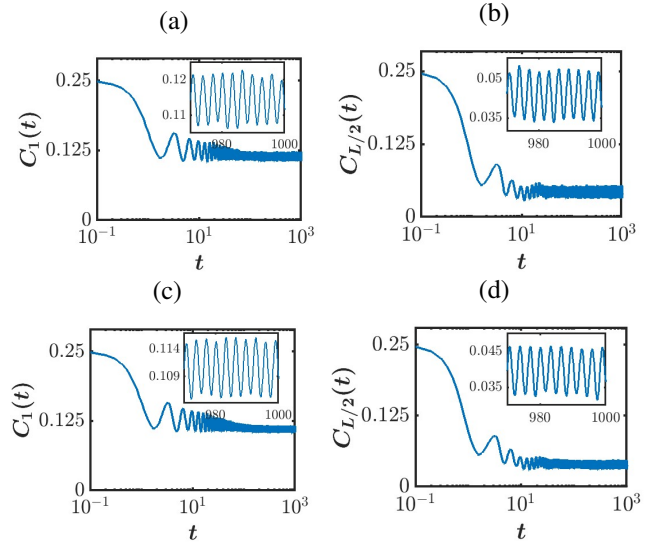


FIG. 11: (a-b) Plots showing the long-time behaviors of the boundary and bulk correlators, $C_1(t)$ and $C_{L/2}(t)$, respectively, starting from a typical random initial state at half-filling with OBC for $L = 18$. (c-d) Similar plots for $L = 20$. (a) $C_1(t)$ oscillates around a finite saturation value of about 0.115 at long times, revealing non-thermal behavior near the boundary of the system. (b) $C_{L/2}(t)$ oscillates around a finite saturation value of about 0.045, which is much smaller than the boundary case. (c) $C_1(t)$ for this case oscillates around a finite saturation of about 0.113 at long times, which is slightly smaller compared to that observed in Fig. (a). (d) In this case, $C_{L/2}$ again shows similar behavior as Fig. (b), but it oscillates around a saturation value (~ 0.04), again slightly smaller compared to Fig. (b). In all four cases, the last ten oscillations for $970 \leq t \leq 1000$ are shown in the insets of the plots.

isfy the inequality due to Mazur⁴⁷

$$F_j \geq \sum_i \frac{(\text{Tr}[P_i(n_j - \frac{1}{2})P_i])^2}{DD_i} \equiv C_j(\infty), \quad (17)$$

Here D_i is the dimensionality of the i -th fragment, and D is the total Hilbert space dimension (here $D = 2^N$).

In Fig. 13 (a), we plot the variation of the infinite-time saturation value of boundary and bulk autocorrelation functions, $C_1^M(\infty)$ and $C_{L/2}^M(\infty)$, obtained using Eq. (17) for an L -site system with OBC. We find that the Mazur bound in the bulk of the chain decays as $1/L$ for comparatively large system sizes like the assisted pair-flipping model. On the other hand, the Mazur bound at the boundary of the chain saturates to approximately 0.12. We show the Mazur bound as a function of the site index for different system sizes in Fig. 13 (b); this shows a non-uniform profile, being smaller at the centre compared to the ends. Further, HSF leads to localization close to the edge of the chain which has been dubbed as ‘‘statistical edge localization’’^{20,21}; we see this in the long-time behavior of boundary autocorrelation functions shown in Figs. 11 (a) and (b). We note here that the late-time average of the bulk autocorrelator decaying with system size as $1/L$ usually indicates thermal behavior of the bulk states. On the other hand,

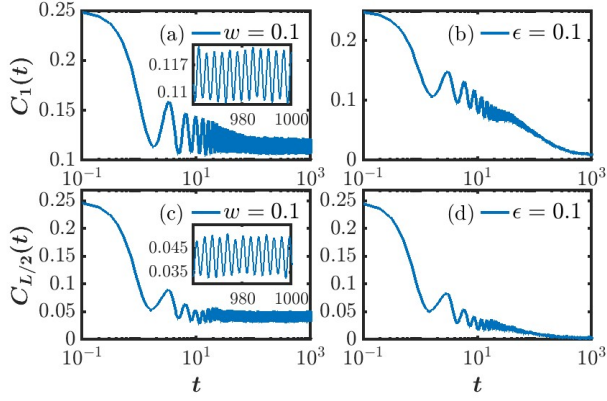


FIG. 12: (a-b) Plots showing the long-time behavior of the boundary correlator $C_1(t)$ starting from a typical random initial state for $L = 18$ at half-filling with OBC in the presence of two kinds of perturbations, uniformly distributed random disorder with disorder strength $w = 0.1$, and the perturbation term with $\epsilon = 0.1$ shown in Eq. (16). (a) $C_1(t)$ oscillates around a finite value of about 0.12 in the long-time limit just as in the unperturbed case. (b) $C_1(t)$ decays to zero at long times after exhibiting a non-trivial intermediate-time dynamics close to the saturation value of the unperturbed model. (c-d) Plots showing the long-time behaviors of bulk correlators, $C_{L/2}(t)$ starting from a random initial state again for the same two cases. (c) $C_{L/2}(t)$ in the presence of random disorder again shows a behavior similar to the unperturbed case. (d) $C_{L/2}(t)$ for this case decays to zero at long times, after exhibiting non-trivial intermediate-time dynamics like the boundary case. In Figs. (a) and (c), the last ten oscillations for $970 \leq t \leq 1000$ are shown in the insets of the plots.

the localized profile of the autocorrelator near the edge shows non-thermal nature of the boundary spectrum. This implies that the non-local conserved quantities arising due to HSF do not have any significant impact on the thermal behavior of the bulk states for our model, in contrast to the boundary states. However, this numerical observation requires a more careful investigation since our analysis has only been carried out for rather small system sizes. In some cases, it has been observed that such thermal behavior of the bulk autocorrelators is an artifact of limited system sizes, and the decay can deviate significantly from $1/L$ in the thermodynamic limit. Specifically, the decay can go as $1/L^a$ where $a < 1^{57}$.

B. Dynamics of entanglement entropy

To complement our previous findings, we study the dynamics of the entanglement entropy starting from the Neel state $101010\dots$ for three different system sizes, $L = 18, 20$ and 22 with OBC. This is shown in Fig. 14 (a). For all three cases, we see that the entanglement entropy quickly saturates to a volume law as shown in Fig. 14 (b). Moreover, the saturation value is much smaller than the thermal value of the entropy of the full system, i.e., $S_{page} = (L \ln 2 - 1)/2^{50}$. The saturation value for all three cases are found to be quite close to the value of the entanglement entropy obtained for a random

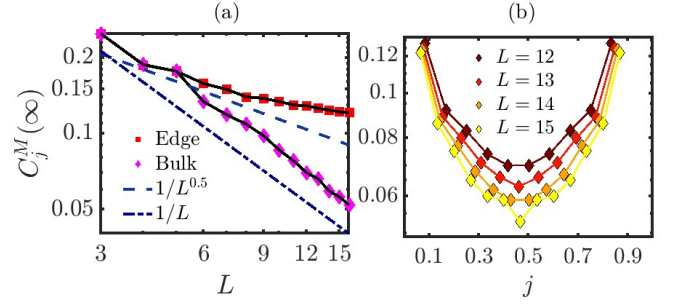


FIG. 13: (a) Log-log plot showing the lower bounds of the infinite-time boundary and bulk correlators predicted by the Mazur inequality for different system sizes. In the bulk of the chain, the Mazur bound follows a $1/L$ curve instead of $1/\sqrt{L}$ (as depicted by two guiding lines), while near the edge of the chain, the Mazur bound shows a localized behavior and saturates to approximately 0.12. (b) The variation of the Mazur bound across the chain for different sizes exhibits a non-uniform profile due to the strong HSF in our model.

state on the full Hilbert space within the largest HSF sector, as depicted by the three dashed lines. These observations are in agreement with our previous findings, i.e., the largest fragment obeys a weaker form of subsector-restricted ETH²⁴.

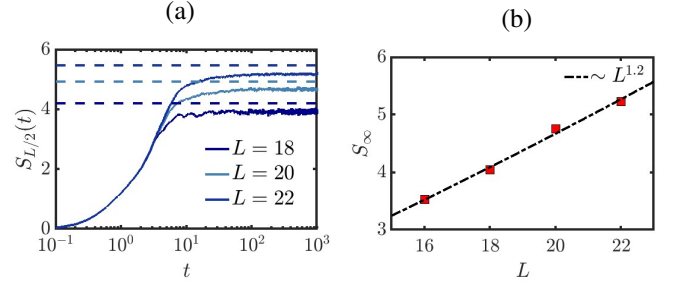


FIG. 14: (a-b) Growth of entanglement entropy with time for three different system sizes, $L = 18, 20$ and 22 with OBC, starting from the Neel state, $101010\dots$. In all three cases, the entanglement entropy quickly saturates to a volume law as shown in Fig. (b), which is much smaller than the thermal value of the entropy for the full system, $S_{page} = (L \ln 2 - 1)/2$. The saturation values for all three cases are very close to the entanglement for a random initial state in the Hilbert space within largest fragment, depicted by the three dashed lines in Fig. (a).

VI. CORRELATED-HOPPING MODEL AS THE LARGE INTERACTION LIMIT OF A $t - V$ MODEL

In this section, we will show that our correlated-hopping model involving terms with four consecutive sites can be obtained by taking a particular large interaction limit of a model of spinless fermions. We consider a model with a nearest-neighbor hopping which we will set equal to 1, and nearest-neighbor density-density interaction terms and on-site potentials which repeat with a periodicity of four sites.

We consider the Hamiltonian

$$H_4 = \sum_j [c_j^\dagger c_{j+1} + c_{j+1}^\dagger c_j + V_j (2n_j - 1)(2n_{j+1} - 1)], \quad (18)$$

where V_j varies with j with period four, namely, $V_{4j+1} = V_1$, $V_{4j+2} = V_2$, $V_{4j+3} = V_3$ and $V_{4j+4} = V_4$. We now consider various correlated-hopping processes involving four consecutive sites, namely, $1101 \leftrightarrow 1011$, $0100 \leftrightarrow 0010$, $1100 \leftrightarrow 1010$ and $0101 \leftrightarrow 0011$, for two different interaction patterns which are related to each other through translation by one site. We list the energy costs for the left and right sides of these correlated-hopping processes in the limit

$V_1, V_2, V_3, V_4 \rightarrow \infty$ in Table V. We see from the table that the interaction energy costs will be equal for the left hand and right hand sides of the processes in rows 3, 4, 6 and 7 (where the occupation numbers n_j are unequal on the first and fourth sites) if $V_1 = -V_3 = V$ and $V_2 = -V_4 = V'$. Simultaneously, the interaction energies will *not* be equal for the left hand and right hand sides of the processes in rows 1, 2, 5 and 6 (where the occupation numbers are equal on the first and fourth sites) if $V, V' \neq 0$. Hence, in the limit $V \rightarrow \pm\infty$ and $V' \rightarrow \pm\infty$, hopping between sites $j+1$ and $j+2$ is allowed if and only if $n_j \neq n_{j+3}$. Note that V and V' can differ from each other in general.

Pattern of V_j	Correlated-hopping process	Energy cost for left hand side of the process in the second column	Energy cost for right hand side of the process in the second column
$V_1 V_2 V_3 V_4$	$1101 \leftrightarrow 1011$	$V_1 - V_2 - V_3$	$-V_1 - V_2 + V_3$
$V_1 V_2 V_3 V_4$	$0100 \leftrightarrow 0010$	$-V_1 - V_2 + V_3$	$V_1 - V_2 - V_3$
$V_1 V_2 V_3 V_4$	$1100 \leftrightarrow 1010$	$V_1 - V_2 + V_3$	$-V_1 - V_2 - V_3$
$V_1 V_2 V_3 V_4$	$0101 \leftrightarrow 0011$	$-V_1 - V_2 - V_3$	$V_1 - V_2 + V_3$
$V_2 V_3 V_4 V_1$	$1101 \leftrightarrow 1011$	$V_2 - V_3 - V_4$	$-V_2 - V_3 + V_4$
$V_2 V_3 V_4 V_1$	$0100 \leftrightarrow 0010$	$-V_2 - V_3 + V_4$	$V_2 - V_3 - V_4$
$V_2 V_3 V_4 V_1$	$1100 \leftrightarrow 1010$	$V_2 - V_3 + V_4$	$-V_2 - V_3 - V_4$
$V_2 V_3 V_4 V_1$	$0101 \leftrightarrow 0011$	$-V_2 - V_3 - V_4$	$V_2 - V_3 + V_4$

TABLE V: Energy costs arising from the V_j term in Eq. (18) for the left and right sides of various correlated-hopping processes for two sets of patterns of V_j related to each other through translation by one site in the limit $V_1, V_2, V_3, V_4 \rightarrow \infty$.

Our analysis thus puts forward an experimentally realizable model which reduces to the four-site correlated-hopping model in the large interaction limit. Namely, we have to consider a model for which the Hamiltonian is given by Eq. (18), with

$$\begin{aligned} V_{4j+1} &= -V_{4j+3} = V, \\ \text{and } V_{4j+2} &= -V_{4j+4} = V'. \end{aligned} \quad (19)$$

Before ending this section we would like to point out that our correlated-hopping model can also emerge as an effective Hamiltonian due to an interplay between dynamical localization, resonance and interactions in a periodically driven system with an on-site potential with a spatial periodicity of four sites³⁹.

VII. COMPARISON WITH A DIFFERENT MODEL SHOWING HILBERT SPACE FRAGMENTATION

It is interesting to contrast various results for our model and a different model showing HSF which has been studied extensively^{20,24,28,29}. This is again a one-dimensional model with spinless fermions but with a Hamiltonian

$$H_5 = \sum_j [1 - (n_j - n_{j+3})^2] (c_{j+1}^\dagger c_{j+2} + c_{j+2}^\dagger c_{j+1}). \quad (20)$$

This Hamiltonian connects the following pairs of states involving four consecutive sites,

$$\begin{aligned} 1101 &\leftrightarrow 1011 \\ 0100 &\leftrightarrow 0010. \end{aligned} \quad (21)$$

This comparison is particularly relevant for our study since this model is also a correlated-hopping model involving four consecutive sites just like ours. However, this model allows nearest-neighbor hoppings if the sites to the left and right of

those two sites have equal particle numbers, unlike our model which enables nearest-neighbor hoppings if the sites to the left and right have different particle numbers. Defining $n_j = c_j^\dagger c_j$ as before, we find that there are three global symmetries: total particle number C_1 , and two other quantities C_4 and C_5 given by

$$\begin{aligned} C_1 &= \sum_j n_j, \\ C_4 &= \sum_j n_{2j} n_{2j+1}, \\ C_5 &= \sum_j n_{2j-1} n_{2j}. \end{aligned} \quad (22)$$

As pointed out in Refs. 30-31, this model can be mapped to a model with a Hamiltonian which involves three consecutive sites. On doing the mapping in Eq. (4), we obtain a model where only the following transitions are allowed,

$$110 \leftrightarrow 011. \quad (23)$$

The Hamiltonian of this model is

$$H_6 = \sum_j n_{j+1} (d_j^\dagger d_{j+2} + d_{j+2}^\dagger d_j), \quad (24)$$

where $n_j = d_j^\dagger d_j$. This Hamiltonian is number conserving, unlike the Hamiltonian in Eq. (6). Note, however, that the total particle numbers $\sum_j n_j$ for the models in Eqs. (20) and (24) are not related to each other in any simple way.

It turns out that a transition of the form given in Eq. (23) was studied many years ago in a classical model of diffusing dimers undergoing Markov evolution⁴³. In that work, a complete solution for the numbers and sizes of fragments was found. For large system sizes, it was shown that the number of fragments grows exponentially as τ^L . The number of frozen sectors is also found to grow as τ^L ,³⁹ unlike our model where it grows as 1.466^L . Further, it was shown in Ref. 43 that for a system with OBC, the different fragments can be characterized uniquely by the numbers of three kinds of short strings, namely, N_A strings given by 11, N_B given by 10, and N_C given by 0. The number of states in a fragment (N_A, N_B, N_C) was shown to be

$$D_{N_A, N_B, N_C} = \frac{(N_A + N_B + N_C)!}{N_A! (N_B + N_C)!}. \quad (25)$$

For a system with L sites, we must have $2N_A + 2N_B + N_C = L$. The filling fraction of particles is given by $(2N_A + N_B)/L$. The frozen fragments with $D_{N_A, N_B, N_C} = 1$ correspond to either $N_A = 0$ and $2N_B + N_C = L$, or $N_A = L/2$ and $N_B = N_C = 0$ (i.e., a string of L 1's).

We can now find how the number of states in an arbitrary fragment grows with L . We define

$$\alpha = \frac{N_A}{L}, \quad \beta = \frac{N_B}{L}, \quad \gamma = \frac{N_C}{L}. \quad (26)$$

These parameters satisfy $\alpha, \beta, \gamma \geq 0$, and $2\alpha + 2\beta + \gamma = 1$. Eliminating β , we see that the parameters (α, γ) lie in a triangular region which is bounded by the lines $\alpha = 0, \gamma = 0$ and $2\alpha + \gamma = 1$ (where $\beta = 0$). We now consider the limit $L \rightarrow \infty$ holding α, β, γ fixed. Using Eq. (25) and Stirling's approximation, we find that the number of states grows as μ^L , where μ is a function of α, γ given by

$$\mu(\alpha, \gamma) = \frac{(\frac{1}{2} + \frac{\gamma}{2})^{(1+\gamma)/2}}{\alpha^\alpha (\frac{1}{2} + \frac{\gamma}{2} - \alpha)^{(1+\gamma-2\alpha)/2}}. \quad (27)$$

We thus see that $\mu(\alpha, \gamma)$ varies continuously over the triangular region. The minimum value of $\mu(\alpha, \gamma)$ is equal to 1; this occurs on the line $(\alpha = 0, 0 \leq \gamma \leq 1)$, and at the point $(\alpha = 1/2, \gamma = 0)$. We will now find the maximum value of $\mu(\alpha, \gamma)$. A numerical search shows that $\mu(\alpha, \gamma)$ attains its maximum on the line $2\alpha + \gamma = 1$. On that line, Eq. (27) simplifies to

$$\mu(\alpha) = \frac{(1 - \alpha)^{1-\alpha}}{\alpha^\alpha (1 - 2\alpha)^{1-2\alpha}}, \quad (28)$$

where $0 \leq \alpha \leq 1/2$. We find analytically that this has a maximum at

$$\alpha = \frac{1}{2} \left(1 - \frac{1}{\sqrt{5}}\right) \simeq 0.2764, \quad (29)$$

where $\mu = \tau$. The filling fraction at this point is $2\alpha \simeq 0.5528$.

Finally, we study if there is a $t - V$ model similar to the one discussed in Sec. VI which reduces to Eq. (20) in the large interaction limit. We consider a model of the form

$$H_7 = \sum_j [c_j^\dagger c_{j+1} + c_{j+1}^\dagger c_j + V_j n_j n_{j+1}], \quad (30)$$

where we again take V_j to vary with j with period four. We carry out an analysis of the energy costs for the left and right hand sides of Eq. (21) similar to the one shown in Table V. We then find that the energy costs on the two sides of Eq. (21) are equal if $V_1 = V_3 = V$ and $V_2 = V_4 = V'$, where V, V' are independent parameters. (Thus the interactions V_j have a period-two structure rather than period-four). In the limit $V \rightarrow \pm\infty$ and $V' \rightarrow \pm\infty$, hopping between sites $j + 1$ and $j + 2$ will be allowed if and only if $n_j = n_{j+3}$.

Finally, we note that if $V = V'$, i.e., $V_j = V$ for all j , the model in Eq. (30) becomes the standard $t - V$ model, and it is exactly solvable by the Bethe ansatz for a system with PBC⁵⁸. However, if $V \neq V'$, it is not known if the model is exactly solvable. In the limit $V = V' \rightarrow \infty$, the model is called the folded XXZ model, and this has also been solved by the Bethe ansatz^{30,31}.

VIII. DISCUSSION

We begin by summarizing our main results. We studied a one-dimensional correlated-hopping model of spinless fermions with terms involving four consecutive sites having a

few global symmetries. This can be mapped to an assisted pair-flipping model with terms involving three consecutive sites. We found that this model shows strong HSF in a particle number basis, and time evolution starting from an arbitrary basis state does not always lead to thermalization. In characterizing the HSF in this model, we found it useful to define IS, analogous to the constructions used earlier^{42,43}. The IS provide us with an exponentially large number of conserved quantities which completely characterize the structure of the HSF. Using the IS, we determined the total number of fragments, the number of frozen states, and the growth of the size of the largest fragment with the system size. These results were also verified using transfer matrix methods and explicit enumerations.

We found that the energy level spacing distribution of the eigenspectrum is approximately Poissonian, but the Hamiltonian within the largest fragment shows approximately GOE level statistics. Our study of infinite-temperature autocorrelation functions and entanglement dynamics also indicated the non-thermal behavior of our model. Further, the finite-size Mazur bound analysis of infinite-temperature autocorrelation functions near one end and inside the bulk of the system pointed towards a thermal bulk spectrum with a non-thermal boundary behavior. We also compared our results with another correlated-hopping model involving four consecutive sites, which has been extensively studied in the context of HSF. Finally, we showed how our correlated-hopping model can be realized in an experimental setting using a variant of the $t - V$ model of spinless fermions in a particular limit.

In brief, we have considered a model in which the basis states are products of local two-dimensional Hilbert spaces. In this basis, the Hamiltonian has a block diagonal structure due to the existence of an infinite number of conserved quantities given by IS. A given block (fragment) may be typical or atypical. In a typical fragment, the expectation values of local observables for most eigenstates at a particular energy tend to the equilibrium values within that fragment. We have called this a subspace-restricted weak ETH.

We end by suggesting possible directions for future research. It would be useful to determine exactly how fast different fragments grow with system size for an arbitrary filling fraction in our model, similar to Eq. (25) which is known for the diffusing dimer model⁴³. It would also be interesting to understand better the large number of zero energy states in the largest fragment (in particular, to see if some of them qualify as many-body scars), and to check if such zero-energy states exist in other large fragments as well. The transport properties vary significantly in different fragments, and it would be useful to understand this better^{27,59-61}. The behaviors of bulk and boundary autocorrelation functions for a typical random thermal state in the thermodynamic limit need to be investigated⁵⁷. Finally, it would be useful to study the effects of disorder^{28,53} and dissipation⁶² in this model. It would also be interesting to see if the concept of IS can be generalized to models where HSF occurs in an entangled basis rather than in a product state in the particle number basis.

We expect that our results can be experimentally tested in cold-atom platforms^{63,64} where spinless fermionic chains with

spatially periodic potentials and strong interactions can be realized. Recently, thermalization in some particular fragments of a model with HSF has been observed in a Rydberg atom system in one dimension⁶⁵. Another observation of HSF has been reported in a superconducting processor in a system exhibiting Stark many-body localization⁶⁶.

Acknowledgments

S.A. thanks MHRD, India for financial support through a PMRF. D.S. thanks SERB, India for funding through Project No. JBR/2020/000043.

Appendix A: Calculation of number of fragments

In this Appendix, we will show how the number of fragments can be calculated using a transfer matrix method. As we have discussed earlier, IS cannot contain the substrings of 1111 and 010. This leads us to construct the following 8×8 transfer matrix $T(C_i, C_j)$ in which the rows and columns C_i and C_j denote configurations of three consecutive sites labelled as 111, 110, 101, 100, 011, 010, 001 and 000. We then have

$$T = \begin{pmatrix} 0 & 1 & 0 & 0 & 0 & 0 & 0 & 0 \\ 0 & 0 & 1 & 1 & 0 & 0 & 0 & 0 \\ 0 & 0 & 0 & 0 & 1 & 0 & 0 & 0 \\ 0 & 0 & 0 & 0 & 0 & 0 & 1 & 1 \\ 1 & 1 & 0 & 0 & 0 & 0 & 0 & 0 \\ 0 & 0 & 0 & 0 & 0 & 0 & 0 & 0 \\ 0 & 0 & 0 & 0 & 1 & 0 & 0 & 0 \\ 0 & 0 & 0 & 0 & 0 & 0 & 1 & 1 \end{pmatrix}. \quad (\text{A1})$$

The eigenvalues of T are analytically found to be τ , $-1/\tau$, $\pm i$ and 0 (which has an algebraic multiplicity of 4), where $\tau = (\sqrt{5} + 1)/2 \simeq 1.618$ is the golden ratio. (The four non-zero eigenvalues are the roots of the quartic equation $z^4 - z^3 - z - 1 = 0$).

Table I shows that $M(n) = M(n-1) + M(n-2)$ for $n \geq 4$. We can use this recursion relation to show that

$$M(n) = \tau^{n+1} + \left(-\frac{1}{\tau}\right)^{n+1}, \quad (\text{A2})$$

for $n \geq 2$. (Note that only two of the non-zero eigenvalues of T appear in Eq. (A2)). In fact, Eq. (A2) holds even for $n = 0$. But for $n = 1$, the right hand side of Eq. (A2) gives 3, while a simple counting shows that $M(1)$ is equal to 2. We now define the generating function for $M(n)$ as

$$G(z) = \sum_{n=0}^{\infty} M(n)z^n. \quad (\text{A3})$$

Using the values of $M(n)$ given above, and summing the se-

ries in Eq. (A3) we obtain

$$G(z) = \frac{\tau}{1 - z\tau} - \frac{1}{\tau + z} - z. \quad (\text{A4})$$

Given the values of $M(n)$ in Table I and Eq. (A2), we find that the number of fragments for a system with L sites and OBC is

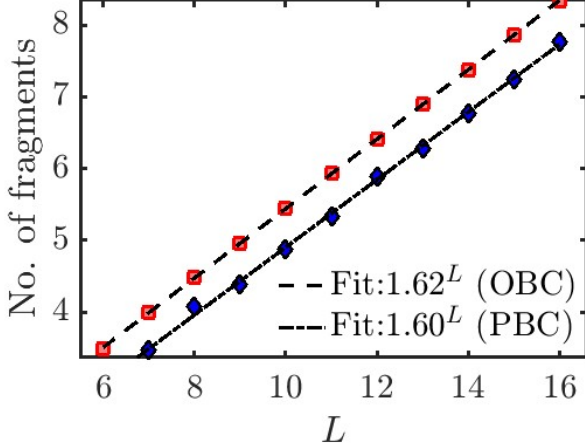


FIG. 15: Number of fragments (on a log scale) versus L for OBC and periodic boundary condition (PBC). The numerical fittings show that the numbers grow approximately as 1.62^L and 1.60^L for OBC and PBC, respectively.

In Fig. 15, we plot the number of fragments N_{frag} versus L for both OBC and PBC. In both cases, we see that N_{frag} grows exponentially as 1.62^L and 1.60^L , which are consistent with the analytically estimated value of τ^L for OBC.

We note that in our numerical work, positive random hoppings uniformly distributed in the range $[1, 2]$ have been used while counting the total number of fragments with PBC in order to avoid any accidental cancellations of sums of matrix elements of the Hamiltonian. As an example of an accidental cancellation, consider $L = 4$ with PBC. Then the state $|1010\rangle$ (which denotes the occupation numbers at sites 1, 2, 3, 4) can go to $|1111\rangle$ in two possible ways, by the action of either $n_3 d_2^\dagger d_4^\dagger$ or $n_1 d_4^\dagger d_2^\dagger$. These two terms cancel each other due to the anticommutation relation $d_2^\dagger d_4^\dagger + d_4^\dagger d_2^\dagger = 0$, which would imply that $|1010\rangle$ and $|1111\rangle$ belong to different fragments.

Appendix B: Calculation of number of frozen states

In this Appendix, we will show how the number of frozen states can be calculated. Unlike the matrix T defined in Eq. (A1) which is designed to remove the configurations 010 and 111, we now need to remove the configurations 010 and 111 in order to find states which are not connected to any other states (and are therefore frozen). We find that the required transfer matrix is a 4×4 matrix whose rows and columns are

labelled as 11, 10, 01 and 00. The required matrix is then

$$T_1 = \begin{pmatrix} 0 & 1 & 0 & 0 \\ 0 & 0 & 1 & 1 \\ 1 & 0 & 0 & 0 \\ 0 & 0 & 1 & 1 \end{pmatrix}. \quad (\text{B1})$$

We discover that one of the eigenvalues of T_1 is zero, while the other three are solutions of the cubic equation

$$\lambda^3 - \lambda^2 - 1 = 0. \quad (\text{B2})$$

The solutions of this equation are given by

$$\lambda = \frac{1}{3} + \frac{2}{3} \cos \left[\frac{1}{3} \cos^{-1} \left(\frac{29}{2} \right) - \frac{2\pi k}{3} \right], \quad (\text{B3})$$

where k can take the values 0, 1, 2. We then find the three eigenvalues to be 1.466 and $-0.233 \pm 0.793i$ approximately; the magnitudes of the last two eigenvalues are less than 1. Hence, the number of frozen states increases asymptotically as 1.466^L . Note that this is a slower growth than the total number of fragments which increases as 1.618^L .

The number of frozen states can also be counted using the fact that the number of such states, $N_{frozen}(L)$, with OBC is given by the sum of all the matrix elements of T_1^{L-2} , for $L \geq 3$. Defining $Y = T_1^{L-2}$, we have

$$N_{frozen} = \sum_{i,j=1}^4 Y_{i,j}. \quad (\text{B4})$$

The counting of frozen states with PBC is slightly different since we have to take care of the constraint that the states of the four consecutive sites $(L-1, L, 1, 2)$ should not contain either 111 or 010. Therefore, defining $Y = T_1^{L-2}$ and taking into account this additional constraint, we find that

$$\begin{aligned} N_{frozen}(L) = & Y(1, 2) + Y(1, 4) + Y(2, 3) \\ & + Y(3, 1) + Y(3, 2) + Y(3, 4) \\ & + Y(4, 1) + Y(4, 3) + Y(4, 4). \end{aligned} \quad (\text{B5})$$

The number of frozen states for first few system sizes shown in Table III exactly agree with the numerically obtained numbers. We note again that for PBC, we have used random hoppings which are uniformly distributed in the range $[1, 2]$ to numerically compute the number of frozen states to avoid any accidental cancellations between different matrix elements of the Hamiltonian.

Appendix C: Calculation of the size of the largest fragment of the three-spin model

We have seen that there are exponentially many frozen fragments which have only one state each. Fragments containing n blinkers have size 2^n . However, there are other fragments which are much larger in size. We typically find that larger

fragments correspond to IS with shorter length (see Fig. 4). We will now study the largest fragments whose IS turn out to consist of either the null string (ϕ), 1, 11 or 111.

We will use the method of enumerative combinatorics of characters⁴¹⁻⁴⁴ to evaluate the size of the fragments of the three-spin model with OBC whose IS consist of only ϕ or 1's. For clarity, we will use the symbols A and B , rather than 0 and 1, to denote the two characters.

We define four formal infinite sums, U_0 , U_1 , U_2 and U_3 as sums of all distinct strings made of characters A and B that correspond to IS which can be ϕ , B , B^2 or B^3 , respectively. We assign a weight x and y to each occurrence of A and B , and the weight of a string having p number of B 's and q number of A 's is $x^p y^q$. We denote the sum of weights of these formal series by $U_0(x, y)$, $U_1(x, y)$, $U_2(x, y)$ and $U_3(x, y)$.

In the sum of terms $U_0(x, y)$, there are terms which contain no A 's and only $4r$ B 's, and other terms, which have an even number of A 's, must have the following structure:

$$U_0 = \frac{\phi}{1-B^4} + \sum_{r=0,1,2,3} \sum_X \frac{B^r}{1-B^4} AWA X, \quad (\text{C1})$$

where W is the sum over all possible substrings of between A 's that reduce to B , so that AWA reduces to ABA and therefore to B^3 . Moreover, X must be reducible to B^s such that $r + 3 + s \equiv 0 \pmod{4}$. Then writing the different possibilities of $r \pmod{4}$ explicitly, we obtain

$$\begin{aligned} U_0 &= \frac{\phi}{1-B^4} + \frac{\phi}{1-B^4} AWA U_1 \\ &+ \frac{B}{1-B^4} AWA U_0 + \frac{B^2}{1-B^4} AWA U_3 \\ &+ \frac{B^3}{1-B^4} AWA U_2. \end{aligned} \quad (\text{C2})$$

Then the generating function U_0 in Eq. (C2) is given by

$$\begin{aligned} U_0(x, y) &= \frac{1}{1-x^4} + \frac{y^2}{1-x^4} W(x, y) U_1(x, y) \\ &+ \frac{xy^2}{1-x^4} W(x, y) U_0(x, y) \\ &+ \frac{x^2 y^2}{1-x^4} W(x, y) U_3(x, y) \\ &+ \frac{x^3 y^2}{1-x^4} W(x, y) U_2(x, y), \end{aligned} \quad (\text{C3})$$

where $W(x, y)$ denotes the weight of W . Since AWA must reduce to B^3 , it must contain an even number of A 's, and $y^2 W(x, y)$ must have terms of the form $x^r y^{2s}$ where $r + 2s = 3 \pmod{4}$, $r \geq 1$, and $s \geq 1$. Hence we can write

$$y^2 W(x, y) = xy^2 H(x, y), \quad (\text{C4})$$

where $H(x, y)$ has terms of the form $x^p y^{2q}$ where $p + 2q = 0 \pmod{4}$.

In a similar manner, one can show that the generating func-

tions U_1 , U_2 and U_3 can be written as

$$\begin{aligned} U_1(x, y) &= \frac{x}{1-x^4} + \frac{xy^2}{1-x^4} W(x, y) U_1(x, y) \\ &+ \frac{y^2}{1-x^4} W(x, y) U_2(x, y) \\ &+ \frac{x^3 y^2}{1-x^4} W(x, y) U_3(x, y) \\ &+ \frac{x^2 y^2}{1-x^4} W(x, y) U_0(x, y), \end{aligned} \quad (\text{C5})$$

$$\begin{aligned} U_2(x, y) &= \frac{x^2}{1-x^4} + \frac{x^3 y^2}{1-x^4} W(x, y) U_0(x, y) \\ &+ \frac{x^2 y^2}{1-x^4} W(x, y) U_1(x, y) \\ &+ \frac{xy^2}{1-x^4} W(x, y) U_2(x, y) \\ &+ \frac{y^2}{1-x^4} W(x, y) U_3(x, y), \end{aligned} \quad (\text{C6})$$

$$\begin{aligned} U_3(x, y) &= \frac{x^3}{1-x^4} + \frac{y^2}{1-x^4} W(x, y) U_0(x, y) \\ &+ \frac{x^3 y^2}{1-x^4} W(x, y) U_1(x, y) \\ &+ \frac{x^2 y^2}{1-x^4} W(x, y) U_2(x, y) \\ &+ \frac{xy^2}{1-x^4} W(x, y) U_3(x, y). \end{aligned} \quad (\text{C7})$$

The generating functions given above can be combined as

$$V(x, y) = U_0(x, y) + U_1(x, y) + U_2(x, y) + U_3(x, y). \quad (\text{C8})$$

Using the identity $(1 + x + x^2 + x^3)/(1 - x^4) = 1/(1 - x)$ and Eq. (C4), we find that

$$V(x, y) = \frac{1}{1 - x - xy^2 H(x, y)}. \quad (\text{C9})$$

We now set $y = x$. Then U_0 , U_1 , U_2 , U_3 will become polynomials in x with terms whose degrees are equal to 0, 1, 2, 3 mod 4, respectively, and $H(x, y) = H(x)$ will become a polynomial in x^4 . We then obtain

$$V(x) = \frac{1}{1 - x - x^3 H(x)}, \quad (\text{C10})$$

where $V(x)$ is the generating function of all strings that reduce to B 's only, and $xH(x)$ is related to IS which reduce to a single B . By direct examination of strings of lengths 0 - 3 (namely, $\phi \rightarrow 1$, $B \rightarrow x$, $BB \rightarrow x^2$, $BBB \rightarrow x^3$ and $ABA \rightarrow xy^2 = x^3$ for $y = x$), we find that the first few

terms in $V(x)$ and $H(x)$ are given by

$$\begin{aligned} V(x) &= 1 + x + x^2 + 2x^3 + \dots, \\ H(x) &= 1 + \dots \end{aligned} \quad (\text{C11})$$

Next, we can write $V(x)$ as

$$V(x) = V_0(x) + x V_1(x) + x^2 V_2(x) + x^3 V_3(x), \quad (\text{C12})$$

where V_0, V_1, V_2 and V_3 are all polynomials in x^4 . Using Eq. (C10) and the fact that V_0, V_1, V_2 and V_3 are polynomials in x^4 , we can show that

$$\begin{aligned} V_0(x) &= \frac{V(x) + V(-x) + V(ix) + V(-ix)}{4}, \\ &= \frac{1 - 2x^4 H}{(1 - 2x^4 H)^2 - x^4(1 + x^4 H^2)^2}, \end{aligned} \quad (\text{C13})$$

$$\begin{aligned} V_1(x) &= \frac{V(x) - V(-x) - iV(ix) + iV(-ix)}{4x}, \\ &= \frac{1 - x^4 + x^8 H^3}{(1 - 2x^4 H)^2 - x^4(1 + x^4 H^2)^2}, \\ V_2(x) &= \frac{V(x) + V(-x) - V(ix) - V(-ix)}{4x^2}, \\ &= \frac{1 + x^4 H^2}{(1 - 2x^4 H)^2 - x^4(1 + x^4 H^2)^2}, \end{aligned} \quad (\text{C14})$$

$$\begin{aligned} V_3(x) &= \frac{V(x) - V(-x) + iV(ix) - iV(-ix)}{4x^3}, \\ &= \frac{1 + H - x^4 H^2}{(1 - 2x^4 H)^2 - x^4(1 + x^4 H^2)^2}. \end{aligned} \quad (\text{C15})$$

Next, we can show that $V_3(x) = 2V_2(x)$ as follows.

1. Given a string in V_2 , one can add a 1 to the left to obtain a string in V_3 . Further, this process is reversible, i.e., given a string in V_3 beginning with 1, one can delete the 1 to obtain a string in V_2 .
2. Next, given a string belonging to V_2 that begins with a 0, one can add a 1 on the right side of the string to obtain a string in V_3 . This process is also reversible: given a string in V_3 which begins with a 0 and ends with a 1, we can delete the 1 to obtain a string in V_2 which begins with a 0.
3. Finally, given a string in V_2 , that begins with a 1, we can replace the 1 by a 0 and add a 0 at the right end of the string. This procedure thus produces a string in V_3 . This mapping is again reversible similar to rules 1 and 2.

Taking $V_3 = 2V_2$ into account and using Eq. (C14) and (C15), we obtain the following quadratic equation for $H(x)$

$$\begin{aligned} 3x^4 H^2 - H + 1 &= 0, \\ \text{which implies } H(x) &= \frac{1 \pm \sqrt{1 - 12x^4}}{6x^4}. \end{aligned} \quad (\text{C16})$$

Eq. (C11) tells us that we have to take the lower sign (minus) in the expression for $H(x)$ in Eq. (C16). We then obtain the

final expression

$$V(x) = \frac{1}{1 - x - \left(\frac{1 - \sqrt{1 - 12x^4}}{6x}\right)}. \quad (\text{C17})$$

This is Eq. (12) in the main text.

Appendix D: Comparison between the growths of the largest fragments in four-site and three-site models

In this section, we compare the sizes of the fragments generated from the root state, $1010 \dots 10$ (or $0101 \dots 01$) of the four-site model with the one generated from the root state, $111 \dots 111$ of the three-site model. Note that both the states $1010 \dots 10$ and $0101 \dots 01$ of the four-site model map to the same state, $111 \dots 111$, of the three-site model under bond-site mapping. We first we compare the cases with OBC. As evinced in Table VI, the sizes of fragments originating from either of the root states $1010 \dots 10$ and $0101 \dots 01$ of the four-site model with L sites are exactly the same as the one obtained from the root state $111 \dots 111$ of the three-site model with $L - 1$ sites. This can be anticipated from the fact that the bond-site mapping mentioned in Sec. II maps two states of the four-site model with L sites to a single state of the three-site model with $L - 1$ sites with OBC.

Next, we compare the fragment sizes for the four-site and three-site models with PBC. We will assume that the system size L is even to take the periodicity of the four-site model into account. As shown in Table VII, the size of the fragment for the root state $1010 \dots 10$ (or $0101 \dots 01$) of the four-site model is two times larger than that of the three-site model for the root state $111 \dots 111$ for $L = 4n$. This is due to the fact that the global symmetries C_2 and C_3 of the four-site model, as discussed in Eq. (3), are well-defined for $L = 4n$, and hence, the states $1010 \dots 10$ and $0101 \dots 01$ lie in the same symmetry sector and belong to a single fragment for a system with PBC. On the other hand, we find that two different fragments arise from the root states $1010 \dots 10$ and $0101 \dots 01$ in the four-site model whose sizes are the same as the single fragment of the three-site model for a chain with $L = 4n + 2$ sites with PBC. We also note that the two root states of the four-site model are not connected to each other by the global symmetries C_2 and C_3 for $L = 4n + 2$, and therefore they generate two different fragments of identical sizes.

Appendix E: Fragmentation structure of the four-site model away from half-filling

We will discuss here strong HSF away from half-filling in our model. In doing so, we consider the following root states of the four-site model with OBC, $\dots 011110011110 \dots$ or $\dots 10001100001 \dots$ which correspond to filling fractions $\nu = 2/3$ and $1/3$ respectively. Both these states map to the state $\dots 101000101000 \dots$ in the three-site model with OBC. Taking this state as a root configuration of the three-site model, we find the dimension of this Hilbert space fragment

L	$D_L^{\text{four-site}}$	$D_L^{\text{three-site}}$
3	1	2
4	2	3
5	3	4
6	4	6
7	12	12
8	12	19
9	19	28
10	28	46
11	46	92
12	92	150
13	150	232
14	232	396
15	396	792
16	792	1315
17	1315	2092
18	2092	3646
19	3646	7292
20	7292	12258
21	12258	19864
22	19864	35076
23	35076	70152
24	70152	118990

TABLE VI: Sizes of fragments generated from the root states $1010 \dots 10$ (or $0101 \dots 01$) and $111 \dots 11$ for the four-site and three-site models respectively, with OBC. We observe that two fragments of identical sizes of the four-site model with L sites maps to a single fragment originated from the root state $1111 \dots 11$ of the three-site model with $L - 1$ sites.

by numerical enumeration for $L = 6, 12, 18$ and 24 ; the results are shown in Table VIII. We have chosen the system sizes to be multiples of 6 to ensure that the pattern of the root state remains invariant as the system size is increased.

In Fig. 16, we show how this fragment grows with L by the numerical enumeration method. Moreover, the numerical fitting indicates that the size of this particular fragment grows as $1.68^L/L^{0.54}$. This again implies that D_i/D goes to zero for $L \rightarrow \infty$, where D being the total dimension of the Hilbert space, which indicates strong HSF²⁵. This observation leads us to conclude that our four-site model exhibits strong HSF²⁵ at arbitrary filling fractions.

In Figs. 17 (a-b), we show the half-chain entanglement entropy as a function of the energy E for the fragment generated from the root state $011110011110 \dots$ at $\nu = 2/3$ for the four-site model with $L = 24$ and OBC; the size of this fragment is 4906. The spectrum shows that most of the eigenstates lie close to a single curve as in a thermal system. Nevertheless, there is also a small fraction of states in the middle of the spec-

L	$D_L^{\text{four-site}}$	$D_L^{\text{three-site}}$
4	6	3
6	10	10
8	38	19
10	106	106
12	300	150
14	1156	1156
16	2630	1315
18	12826	12826
20	24516	12258
22	143980	143980
24	237980	118990
26	1630084	1630084

TABLE VII: sizes of fragments generated from the root configurations $1010 \dots$ (or $0101 \dots 01$) and $111 \dots 111$ for the four-site and three-site model, respectively, with PBC. We note that for $L = 4n$, the two states belong to the same fragment in the four-site model, whereas for $L = 4n + 2$, the four-site model exhibits two different fragments with the same size D_L , one coming from the root configuration $101010 \dots 10$ and the other from $010101 \dots 01$.

L	6	12	18	24
$D_{i,L}$	7	107	1906	35259

TABLE VIII: Size of the fragment $D_{i,L}$ versus L obtained from the root state $101000101000 \dots$ for the three-site model with OBC.

trum with anomalously low entanglement entropy. We further perform an analysis of the energy level statistics within this fragment after adding a small amount of randomly distributed on-site disorder of strength $w = 0.01$ for the same reasons mentioned in Sec. IV. The probability distribution of \tilde{r} within this fragment is found to follow the GOE with $\langle \tilde{r} \rangle \simeq 0.51$, which is close to the GOE value. The fluctuations in the analysis of \tilde{r} arise due to the limited system sizes. Since we want to keep the 01110 pattern of the root state intact while generating this sector, we must take L to be a multiple of six. We have to limit our analysis to $L = 24$ since the next system size $L = 30$ is numerically very difficult. We find that our model always exhibits strong HSF irrespective of the filling unlike models where a transition from strong to weak HSF can occur as a function of the filling fraction^{60,67}.

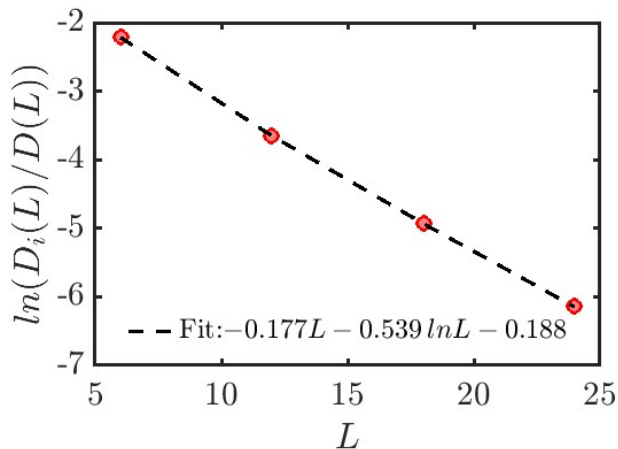


FIG. 16: Plot of the ratio of the size D_i of the fragment of interest to the total dimension $D = 2^L$ of the Hilbert space (shown on a log scale) versus L for a system with OBC. The ratio is seen to decrease exponentially with L .

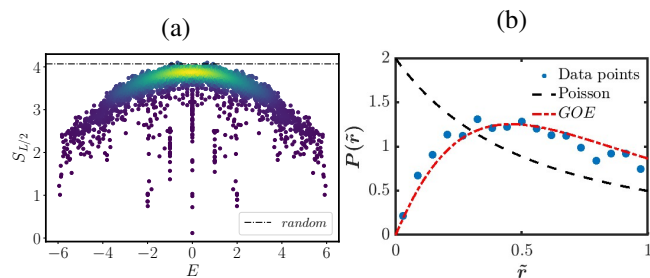


FIG. 17: (a) Plot of $S_{L/2}$ versus E for the fragment generated from the root state, 0111001110... for $L = 24$ at filling fraction $\nu = 2/3$ for the four-site model with OBC. The fragment size is 4906. The dash-dot line indicates the value of the entanglement entropy of a random state in this subspace. The entanglement spectrum contains a small fraction of eigenstates with low entanglement entropy in the middle of the spectrum. (b) The level spacing ratio analysis for the same fragment in the presence of a small uniformly distributed random disorder with disorder strength $w = 0.01$. The probability distribution of \tilde{r} is close to the GOE distribution with $\langle \tilde{r} \rangle \simeq 0.51$.

¹ M. Srednicki, Phys. Rev. E **50**, 888 (1994), URL <https://link.aps.org/doi/10.1103/PhysRevE.50.888>.
² J. M. Deutsch, Phys. Rev. A **43**, 2046 (1991), URL <https://link.aps.org/doi/10.1103/PhysRevA.43.2046>.
³ M. Rigol, V. Dunjko, and M. Olshanii, Nature **452**, 854 (2008), URL <https://doi.org/10.1038/nature06838>.
⁴ A. Polkovnikov, K. Sengupta, A. Silva, and M. Vengalattore, Rev. Mod. Phys. **83**, 863 (2011), URL <https://link.aps.org/doi/10.1103/RevModPhys.83.863>.
⁵ M. Rigol, V. Dunjko, V. Yurovsky, and M. Olshanii, Phys. Rev. Lett. **98**, 050405 (2007), URL <https://link.aps.org/doi/10.1103/PhysRevLett.98.050405>.

⁶ M. Fagotti and F. H. L. Essler, Phys. Rev. B **87**, 245107 (2013), URL <https://link.aps.org/doi/10.1103/PhysRevB.87.245107>.
⁷ T. N. Ikeda, Y. Watanabe, and M. Ueda, Phys. Rev. E **87**, 012125 (2013), URL <https://link.aps.org/doi/10.1103/PhysRevE.87.012125>.
⁸ J.-S. Caux and R. M. Konik, Phys. Rev. Lett. **109**, 175301 (2012), URL <https://link.aps.org/doi/10.1103/PhysRevLett.109.175301>.
⁹ G. Mussardo, Phys. Rev. Lett. **111**, 100401 (2013), URL <https://link.aps.org/doi/10.1103/PhysRevLett.111.100401>.

- ¹⁰ A. Pal and D. A. Huse, Phys. Rev. B **82**, 174411 (2010), URL <https://link.aps.org/doi/10.1103/PhysRevB.82.174411>.
- ¹¹ R. Vosk and E. Altman, Phys. Rev. Lett. **110**, 067204 (2013), URL <https://link.aps.org/doi/10.1103/PhysRevLett.110.067204>.
- ¹² D. A. Huse, R. Nandkishore, V. Oganesyan, A. Pal, and S. L. Sondhi, Phys. Rev. B **88**, 014206 (2013), URL <https://link.aps.org/doi/10.1103/PhysRevB.88.014206>.
- ¹³ R. Nandkishore and D. A. Huse, Annual Review of Condensed Matter Physics **6**, 15 (2015), URL <https://doi.org/10.1146/annurev-conmatphys-031214-014726>.
- ¹⁴ T. Iadecola and M. Schechter, Phys. Rev. B **101**, 024306 (2020), URL <https://link.aps.org/doi/10.1103/PhysRevB.101.024306>.
- ¹⁵ C. J. Turner, A. A. Michailidis, D. A. Abanin, M. Serbyn, and Z. Papić, Nature Physics **14**, 745 (2018), URL <https://doi.org/10.1038/s41567-018-0137-5>.
- ¹⁶ S. Choi, C. J. Turner, H. Pichler, W. W. Ho, A. A. Michailidis, Z. Papić, M. Serbyn, M. D. Lukin, and D. A. Abanin, Phys. Rev. Lett. **122**, 220603 (2019), URL <https://link.aps.org/doi/10.1103/PhysRevLett.122.220603>.
- ¹⁷ S. Moudgalya, N. Regnault, and B. A. Bernevig, Phys. Rev. B **98**, 235156 (2018), URL <https://link.aps.org/doi/10.1103/PhysRevB.98.235156>.
- ¹⁸ C.-J. Lin and O. I. Motrunich, Phys. Rev. Lett. **122**, 173401 (2019), URL <https://link.aps.org/doi/10.1103/PhysRevLett.122.173401>.
- ¹⁹ T. Iadecola, M. Schechter, and S. Xu, Phys. Rev. B **100**, 184312 (2019), URL <https://link.aps.org/doi/10.1103/PhysRevB.100.184312>.
- ²⁰ S. Moudgalya, B. A. Bernevig, and N. Regnault, Reports on Progress in Physics **85**, 086501 (2022), URL <https://dx.doi.org/10.1088/1361-6633/ac73a0>.
- ²¹ T. Rakovszky, P. Sala, R. Verresen, M. Knap, and F. Pollmann, Phys. Rev. B **101**, 125126 (2020), URL <https://link.aps.org/doi/10.1103/PhysRevB.101.125126>.
- ²² S. Moudgalya and O. I. Motrunich, Phys. Rev. X **12**, 011050 (2022), URL <https://link.aps.org/doi/10.1103/PhysRevX.12.011050>.
- ²³ M. Borsi, L. Pristiyák, and B. Pozsgay, Phys. Rev. Lett. **131**, 037101 (2023), URL <https://link.aps.org/doi/10.1103/PhysRevLett.131.037101>.
- ²⁴ S. Moudgalya, B. A. Bernevig, and N. Regnault, Phys. Rev. B **102**, 195150 (2020), URL <https://link.aps.org/doi/10.1103/PhysRevB.102.195150>.
- ²⁵ P. Sala, T. Rakovszky, R. Verresen, M. Knap, and F. Pollmann, Phys. Rev. X **10**, 011047 (2020), URL <https://link.aps.org/doi/10.1103/PhysRevX.10.011047>.
- ²⁶ B. Mukherjee, D. Banerjee, K. Sengupta, and A. Sen, Phys. Rev. B **104**, 155117 (2021), URL <https://link.aps.org/doi/10.1103/PhysRevB.104.155117>.
- ²⁷ P. Brighi, M. Ljubotina, and M. Serbyn, SciPost Phys. **15**, 093 (2023), URL <https://scipost.org/10.21468/SciPostPhys.15.3.093>.
- ²⁸ G. De Tomasi, D. Hetterich, P. Sala, and F. Pollmann, Phys. Rev. B **100**, 214313 (2019), URL <https://link.aps.org/doi/10.1103/PhysRevB.100.214313>.
- ²⁹ V. Khemani, M. Hermele, and R. Nandkishore, Phys. Rev. B **101**, 174204 (2020), URL <https://link.aps.org/doi/10.1103/PhysRevB.101.174204>.
- ³⁰ L. Zadnik and M. Fagotti, SciPost Phys. Core **4**, 010 (2021), URL <https://scipost.org/10.21468/SciPostPhysCore.4.2.010>.
- ³¹ B. Pozsgay, T. Gombor, A. Hutsalyuk, Y. Jiang, L. Pristiyák, and E. Vernier, Phys. Rev. E **104**, 044106 (2021), URL <https://link.aps.org/doi/10.1103/PhysRevE.104.044106>.
- ³² Z.-C. Yang, F. Liu, A. V. Gorshkov, and T. Iadecola, Phys. Rev. Lett. **124**, 207602 (2020), URL <https://link.aps.org/doi/10.1103/PhysRevLett.124.207602>.
- ³³ K. Lee, A. Pal, and H. J. Changlani, Phys. Rev. B **103**, 235133 (2021), URL <https://link.aps.org/doi/10.1103/PhysRevB.103.235133>.
- ³⁴ A. Khudorozhkov, A. Tiwari, C. Chamon, and T. Neupert, SciPost Phys. **13**, 098 (2022), URL <https://scipost.org/10.21468/SciPostPhys.13.4.098>.
- ³⁵ A. Yoshinaga, H. Hakoshima, T. Imoto, Y. Matsuzaki, and R. Hamazaki, Phys. Rev. Lett. **129**, 090602 (2022), URL <https://link.aps.org/doi/10.1103/PhysRevLett.129.090602>.
- ³⁶ O. Hart and R. Nandkishore, Phys. Rev. B **106**, 214426 (2022), URL <https://link.aps.org/doi/10.1103/PhysRevB.106.214426>.
- ³⁷ D. T. Stephen, O. Hart, and R. M. Nandkishore, Phys. Rev. Lett. **132**, 040401 (2024), URL <https://link.aps.org/doi/10.1103/PhysRevLett.132.040401>.
- ³⁸ S. Ghosh, I. Paul, and K. Sengupta, Phys. Rev. Lett. **130**, 120401 (2023), URL <https://link.aps.org/doi/10.1103/PhysRevLett.130.120401>.
- ³⁹ S. Aditya and D. Sen, SciPost Phys. Core **6**, 083 (2023), URL <https://scipost.org/10.21468/SciPostPhysCore.6.4.083>.
- ⁴⁰ L. Zhang, Y. Ke, L. Lin, and C. Lee, arXiv:2311.11771 (2023), URL <https://doi.org/10.48550/arXiv.2311.11771>.
- ⁴¹ M. Barma and D. Dhar, Phys. Rev. Lett. **73**, 2135 (1994), URL <https://link.aps.org/doi/10.1103/PhysRevLett.73.2135>.
- ⁴² M. K. H. Menon and D. Dhar, Journal of Physics A: Mathematical and General **28**, 6517 (1995), URL <https://dx.doi.org/10.1088/0305-4470/28/23/008>.
- ⁴³ G. I. Menon, M. Barma, and D. Dhar, Journal of Statistical Physics **86**, 1237 (1997), URL <https://doi.org/10.1007/BF02183622>.
- ⁴⁴ R. L. Graham, D. E. Knuth, and O. Patashnik, *Chapter 7: Generating Functions*, *Concrete mathematics: a foundation for computer science*. (Amsterdam: Addison-Wesley Publishing Group, 1994), 2nd ed., ISBN 0-201-55802-5.
- ⁴⁵ E. P. Wigner, Annals of Mathematics **62**, 548 (1955), URL <http://www.jstor.org/stable/1970079>.
- ⁴⁶ M. Serbyn, A. A. Michailidis, D. A. Abanin, and Z. Papić, Phys. Rev. Lett. **117**, 160601 (2016), URL <https://link.aps.org/doi/10.1103/PhysRevLett.117.160601>.
- ⁴⁷ P. Mazur, Physica **43**, 533 (1969), ISSN 0031-8914, URL <https://www.sciencedirect.com/science/article/pii/0031891469901852>.
- ⁴⁸ M. Suzuki, Physica **51**, 277 (1971), ISSN 0031-8914, URL <https://www.sciencedirect.com/science/article/pii/0031891471902266>.
- ⁴⁹ W. Beugeling, R. Moessner, and M. Haque, Phys. Rev. E **89**, 042112 (2014), URL <https://link.aps.org/doi/10.1103/PhysRevE.89.042112>.
- ⁵⁰ D. N. Page, Phys. Rev. Lett. **71**, 1291 (1993), URL <https://link.aps.org/doi/10.1103/PhysRevLett.71.1291>.
- ⁵¹ Y. Y. Atas, E. Bogomolny, O. Giraud, and G. Roux, Phys. Rev. Lett. **110**, 084101 (2013), URL <https://link.aps.org/>

- [doi/10.1103/PhysRevLett.110.084101](https://doi.org/10.1103/PhysRevLett.110.084101).
- ⁵² M. V. Berry and M. Tabor, Proceedings of the Royal Society of London. Series A, Mathematical and Physical Sciences **356**, 375 (1977), URL <http://www.jstor.org/stable/79349>.
- ⁵³ L. Herviou, J. H. Bardarson, and N. Regnault, Phys. Rev. B **103**, 134207 (2021), URL <https://link.aps.org/doi/10.1103/PhysRevB.103.134207>.
- ⁵⁴ Y. H. Kwan, P. H. Wilhelm, S. Biswas, and S. A. Parameswaran, arXiv:2304.02669 (2023), URL <https://doi.org/10.48550/arXiv.2304.02669>.
- ⁵⁵ M. Schecter and T. Iadecola, Phys. Rev. B **98**, 035139 (2018), URL <https://link.aps.org/doi/10.1103/PhysRevB.98.035139>.
- ⁵⁶ A. Udupa, S. Sur, S. Nandy, A. Sen, and D. Sen, Phys. Rev. B **108**, 214430 (2023), URL <https://link.aps.org/doi/10.1103/PhysRevB.108.214430>.
- ⁵⁷ O. Hart, arXiv:2308.00738 (2023), URL <https://doi.org/10.48550/arXiv.2308.00738>.
- ⁵⁸ B. Sutherland, *Beautiful Models* (World Scientific, Singapore, 2004).
- ⁵⁹ A. Bastianello, U. Borla, and S. Moroz, Phys. Rev. Lett. **128**, 196601 (2022), URL <https://link.aps.org/doi/10.1103/PhysRevLett.128.196601>.
- ⁶⁰ C. Wang and Z.-C. Yang, Phys. Rev. B **108**, 144308 (2023), URL <https://link.aps.org/doi/10.1103/PhysRevB.108.144308>.
- ⁶¹ M. Barma and D. Dhar, Phys. Rev. Lett. **73**, 2135 (1994), URL <https://link.aps.org/doi/10.1103/PhysRevLett.73.2135>.
- ⁶² S. Ghosh, K. Sengupta, and I. Paul, Phys. Rev. B **109**, 045145 (2024), URL <https://link.aps.org/doi/10.1103/PhysRevB.109.045145>.
- ⁶³ I. Bloch, J. Dalibard, and W. Zwerger, Rev. Mod. Phys. **80**, 885 (2008), URL <https://link.aps.org/doi/10.1103/RevModPhys.80.885>.
- ⁶⁴ T. Kohlert, S. Scherg, P. Sala, F. Pollmann, B. H. Madhusudhana, I. Bloch, and M. Aidelsburger, arXiv:2106.15586 (2021), URL <https://doi.org/10.48550/arXiv.2106.15586>.
- ⁶⁵ L. Zhao, P. R. Datla, W. Tian, M. M. Aliyu, and H. Loh, arXiv:2403.09517 (2024), URL <https://doi.org/10.48550/arXiv.2403.09517>.
- ⁶⁶ Y.-Y. Wang, Y.-H. Shi, Z.-H. Sun, C.-T. Chen, Z.-A. Wang, K. Zhao, H.-T. Liu, W.-G. Ma, Z. Wang, H. Li, et al., arXiv:2403.09095 (2024), URL <https://doi.org/10.48550/arXiv.2403.09095>.
- ⁶⁷ A. Morningstar, V. Khemani, and D. A. Huse, Phys. Rev. B **101**, 214205 (2020), URL <https://link.aps.org/doi/10.1103/PhysRevB.101.214205>.